

Opposing-buoyancy mixed convection through and around arrays of heated cylinders

Tingting Tang^{1,2}, Zhiyong Li^{1,3}, Shimin Yu^{1,4}, Jianhui Li¹ and Peng Yu^{1,2,†}

¹Department of Mechanics and Aerospace Engineering, Southern University of Science and Technology, Shenzhen 518055, PR China

²Center for Complex Flows and Soft Matter Research, Southern University of Science and Technology, Shenzhen 518055, PR China

³Dongguan University of Technology, Dongguan 523808, PR China

⁴Harbin Institute of Technology, Harbin 150001, PR China

(Received 21 August 2021; revised 3 August 2022; accepted 18 August 2022)

We numerically investigated the opposing-buoyancy mixed convection through and around square arrays of 10×10 heated circular cylinders with the solid fraction (ϕ) ranging from 0.0079 to 0.66 and the Richardson number (Ri) varying from 0 to 1 at a fixed Reynolds number (Re) of 100. Our simulations revealed that the large mean recirculation in the far wake can be detached from or connected with the vortex pair in the near wake for different combinations of Ri and ϕ . Also, it was found that the array with relatively small ϕ can significantly promote flow instability even at moderate Ri . The instability, which is closely related to the fluctuating heat flux, develops from the lateral sides to the downstream side of the array and gives rise to the large mean recirculation in the far wake. The power spectra density of the array-scale force coefficients demonstrates that the flow undergoes different bifurcation behaviours under various parameter combinations, which reflects the interaction between the near-wake and far-wake vortices. Interestingly, the Strouhal–Richardson number curves can be collapsed onto the same curve when Ri is increased by a ϕ -dependent factor. Also, for $\phi \leq 0.22$, both the mean drag coefficient and the mean Nusselt number of the array were found to decrease linearly with Ri since the buoyancy within the array becomes prominent in this range of ϕ .

Key words: convection in porous media, buoyancy-driven instability

† Email address for correspondence: yup6@sustech.edu.cn

1. Introduction

Mixed convection around and through a group of bodies or a porous medium is of great significance for various engineering applications such as electronics cooling, micro heat exchangers and fuel cells. As a combination of forced and free convection, the mixed convection has received increasing attention in the past several decades, especially under the effects of aiding, cross and opposing-buoyancy forces, which are respectively in the same, perpendicular and opposite directions with the approaching forced flow. In each of the configurations, the flow and heat transfer are governed by the Richardson number (Ri), Reynolds number (Re) and Prandtl number (Pr).

The influences of the buoyancy force on the flow and heat transfer characteristics are significant. Under the action of aiding thermal buoyancy, vortex shedding can be suppressed and the mean Nusselt number (\overline{Nu}) increases with Ri (Salimipour 2019). Differently, cross-buoyancy promotes the initiation of vortex shedding at a much smaller Re (Chatterjee & Mondal 2011). For unsteady flow, cross-buoyancy significantly alters the flow field in the downstream as well as the upstream regions by injecting fluids into the near-wake region (Mahir & Altaç 2019). Opposing buoyancy is also known to trigger vortex shedding at relatively low Re . However, compared with aiding and cross-buoyancy, much fewer investigations have been conducted on the effects of opposing buoyancy in the unsteady regime.

Most of the previous relevant studies focused on flow around a single solid bluff body. Chang & Sa (1990) numerically studied the phenomenon of vortex shedding from a heated/cooled circular cylinder at $Re = 100$. It was found that the pattern of the ordinary vortex streets can be severely altered by the buoyancy force concerning the structure and size of the vortices. With opposing buoyancy, the strength of the shear layer increases and the roll-up process is more activated. The non-dimensional parameters of Strouhal number (St), \overline{Nu} and mean drag coefficient ($\overline{C_D}$) were all reported to decrease with an increment of the opposing-buoyancy force. Patnaik, Narayana & Seetharamu (1999) studied the influences of buoyancy opposed convection on flow past a circular cylinder at relatively low Reynolds number and found that vortex shedding can be triggered at $Re \in [20, 40]$, where there are only twin vortices without buoyancy. Gandikota *et al.* (2010) studied the effects of opposing buoyancy on the flow around a circular cylinder at $Pr = 0.7$ and Re from 50 to 150 for blocking ratios of 0.25 and 0.02. Both St and \overline{Nu} were found to be larger for higher blockage.

Hu & Koochesfahani (2011) experimentally studied the thermal effects on wake flow behind a heated circular cylinder at $Re = 135$ and $Pr = 7$. It was found that the wake vortex structure varies significantly with Ri . The alternate shedding of ‘Kármán’ vortices is replaced by the formation of smaller wake vortices that are generated almost concurrently at two sides of the heated cylinder for $Ri > 0.72$. The wake closure length and $\overline{C_D}$ initially decrease slightly and then increase monotonically with increasing Ri ; also, \overline{Nu} decreases almost linearly with Ri . The variation trends of St and \overline{Nu} with Ri agreed well with those of Chang & Sa (1990). Guillén, Treviño & Martínez-Suástegui (2014) experimentally studied flow past a cylinder in a confined water channel with opposing buoyancy at $Pr = 7$ and $Re = 170$. The flow pattern was found to be characterized by the presences of the stagnant zone (with almost zero velocity/vorticity at the cylinder rear) and the recirculation zone developed further downstream. The length and width of the recirculation zone both increase with Ri . Also, the measured St is higher than that for an unconfined cylinder.

Apart from circular cylinders, bluff bodies with different cross-sections were also considered. Sharma & Eswaran (2004) numerically studied the influence of opposing

buoyancy on the flow around the more bluff square cylinder at $Re = 100$ and $Pr = 0.7$. The qualitative behaviours of St , $\overline{C_D}$ and \overline{Nu} were consistent with those of circular cylinders. However, the variation trend that the wake closure length decreases with Ri is opposite to the trend reported by Hu & Koochesfahani (2011) and Guillén *et al.* (2014). The reason is that different types of vortexes were detected, which were not differentiated in these studies and will be discussed more in the following sections. Sharma & Eswaran (2005) also studied the effects of channel confinement under similar flow configurations. The enhancements of heat transfer were observed to increase with increasing blockage ratio but decrease with increasing Ri . Sarkar, Ganguly & Dalal (2013) studied the flow of nanofluids past a square cylinder under opposing buoyancy with $Pr = 6.9$ and $Re = 100$. The vortex shedding process is initiated when the nanofluid solid volume fraction is increased. It was demonstrated that \overline{Nu} increases as the nanofluid solid volume fraction increases. Chatterjee & Ray (2014) studied mixed convection with opposing buoyancy over a triangular surface for $Re < 30$ and $Pr = 50$. It was found that St decreases slightly with Ri , similar to those reported in the above-mentioned studies. However, \overline{Nu} was found to increase with Ri , which is opposite to the trends presented by Hu & Koochesfahani (2011) and Sharma & Eswaran (2004).

There are also several studies on flow and heat transfer around and through arrays of a small number of cylinders ($N < 10$) with the effects of opposing buoyancy. Salcedo *et al.* (2017) investigated mixed convection flow from two circular cylinders arranged in tandem and confined in a channel at $Re = 200$ (for an individual cylinder) and $Pr = 7$. The results showed five distinct flow patterns in the parameters space of gap width and opposed buoyancy strength: (1) steady-state flow, (2) time-periodic oscillatory state, (3) quasi-periodic oscillatory flow, (4) bistable flow and (5) chaotic motion. Also, the recirculation zones that form within the gap can exhibit both symmetrical and asymmetrical patterns. It was found that \overline{Nu} of the upstream cylinder decreases with Ri while \overline{Nu} of the downstream cylinder increases with Ri . Fornarelli, Lippolis & Oresta (2017) studied the effects of thermal buoyancy on the flow around an array of six circular cylinders at $Re = 100$ and $Pr = 0.7$. For cases with opposing buoyancy, the spacing affects heavily the oscillation amplitude of the force and heat exchange coefficients. For relatively large spacing, the standard deviation of the performance coefficients increases with Ri ; while for smaller spacing, the flow can rearrange itself in a more ordered wake pattern configuration, limiting the oscillation amplitude of the performance coefficients. It was also shown that \overline{Nu} of the array increases with Ri , which is opposite to the trend of flow around a single cylinder.

As the number of cylinders increases to a certain value, the array begins to resemble a porous medium since the overall effects of the array on the ambient fluid can be represented in terms of a macroscopic drag force (Nicolle & Eames 2011). The approach is widely used (e.g. Zong & Nepf 2012; Taddei, Manes & Ganapathisubramani 2016; Zargartalebi & Azaiez 2019; Chakkingal *et al.* 2020; Liu *et al.* 2020). Nevertheless, the studies on mixed convection around and through a porous body or a group of constituent elements are fairly limited. Vijaybabu, Anirudh & Dhinakaran (2017, 2018) studied steady mixed convection around and through the permeable square and triangular cylinders with aiding buoyancy. Yu, Yu & Tang (2018) considered the effects of both aiding and opposing-buoyancy mixed convection on steady flow past a permeable circular cylinder. Both $\overline{C_D}$ and \overline{Nu} were observed to decrease with Ri .

The present study aims to understand the expectantly more unstable flow and heat transfer characteristics for mixed convection around and through an array of heated cylinders under opposing buoyancy. It is mainly motivated by the findings of the previous

studies (Anirudh & Dhinakaran 2018; Tang *et al.* 2020) that the critical Reynolds number for the onset of vortex shedding behind a permeable body or a group of bodies decreases with decreasing solid fraction (ϕ) in the investigated range of ϕ , which seems contradictory to the common sense as well as the findings that porous media help to stabilize the flow (Ledda *et al.* 2019). Tang *et al.* (2020) concluded that the increased overall instability at relatively small ϕ is mainly caused by the intensified interaction of inertial and viscous forces among individual cylinders in the array. Since the opposing-buoyancy-induced flow interacts with the downward inertial flow within the array, it is expected to further increase the overall instability in the group of bodies. The current work aims to investigate this hypothesis. Besides, the existing limited studies on opposing-buoyancy mixed convection around and through a permeable body mainly considered flow in the steady regime, which may not be plausible since the vortex shedding is easily triggered by the opposed buoyancy force.

The rest of the paper is structured as follows. In § 2 the problem under consideration and the numerical method are described. In § 3 the numerical results are provided in terms of the mean recirculation regions, the force coefficients and the mean heat transfer coefficients. Finally, the summary and conclusions are given in § 4.

2. Numerical method

2.1. Problem definition

The present study considers two-dimensional flow through and around a square array of multiple circular cylinders with various ϕ . Each cylinder is assumed to be connected to a hot source and the thermal resistance between the hot source and the cylinder is assumed to be very small, therefore, the surfaces of the cylinders remain at a hot temperature T_h . The geometry of the computational domain is shown schematically in figure 1(a). The cylinder array with a side length of D is placed at the zero attack angle to the incoming cold flow with uniform velocity (U_∞) and ambient temperature (T_c). The direction of the gravity is parallel to that of the incoming flow, therefore, the buoyancy is opposed to the forced flow direction. Sufficiently large distances are used between the cylinder array and domain boundaries to minimize the effects of the boundaries on the flow. The distances from the array to the left, bottom, right and top boundaries are denoted as N_L , N_B , N_R and N_T , respectively, with N_L , N_R , $N_T = 20D$ and $N_B = 60D$. The blockage ratios of all cases are no greater than 0.0244, which are comparable with those used for flow around a solid square cylinder (Sen, Mittal & Biswas 2011).

The geometries of the cylinder arrays employed in the present simulations are shown in figure 1(b). Each array is composed of 10×10 circular cylinders with an equal diameter (d) and a uniform spacing (s) (see figure 1a). The constituent element is selected to be a circular cylinder as the flow past it has been extensively studied (Zdravkovich 1997). The boundaries of each array (dashed lines) form a square enclosure. The side length of the square enclosure can thus be calculated as $D = (9r + 10)d$, where the spacing-to-diameter ratio (r) is defined as s/d . The solid fraction of the array (ϕ), which is defined as the ratio of the volume of the solid cylinders to the total volume of the square enclosure, is calculated from $\phi = 25\pi(d/D)^2$. The investigated range of ϕ is from 0.00785 to 0.66, corresponding to r decreasing from 10 to 0.1. Each array with the same number of constituent elements can be considered as a porous square cylinder with the same side length. The geometry with $\phi = 1$ represents a single solid square cylinder with a side length of D . The current geometry configuration easily guarantees that the Re of the whole array is the same for all cases.

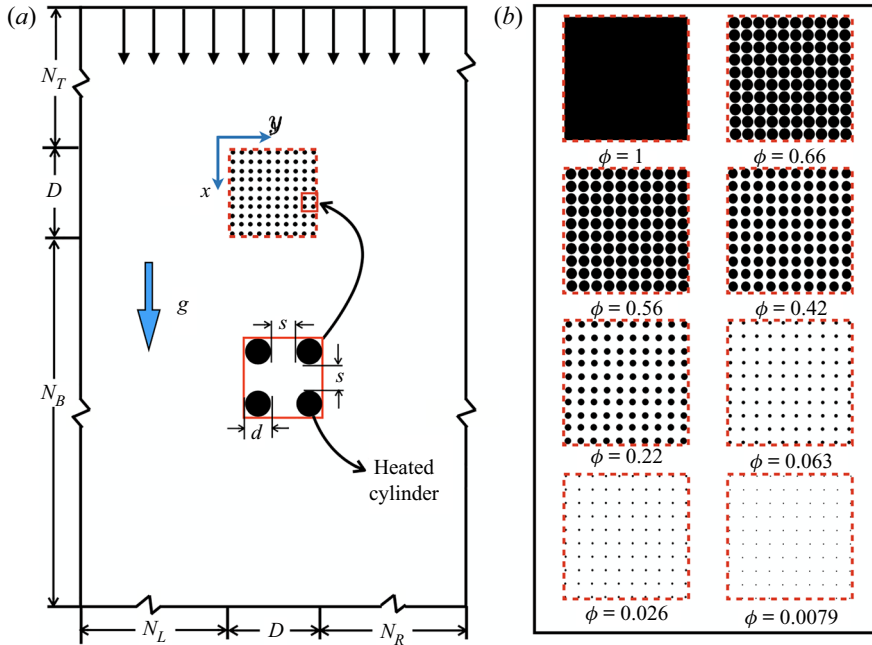


Figure 1. (a) Sketch of the flow problem and the computational domain. (b) Geometric configuration of the array investigated in the present study.

2.2. Governing equations

For incompressible Newtonian fluid flow through and around the cylinder array under the Boussinesq approximation, the governing equations of mass, momentum and energy conservations are expressed as

$$\nabla \cdot \mathbf{u} = 0, \tag{2.1a}$$

$$\frac{\partial \mathbf{u}}{\partial t} + \mathbf{u} \cdot \nabla \mathbf{u} = -\frac{1}{\rho_0} \nabla p + \nu \Delta \mathbf{u} - \mathbf{g} \beta (T - T_c), \tag{2.1b}$$

$$\frac{\partial T}{\partial t} + \mathbf{u} \cdot \nabla T = k/(\rho_0 c) \Delta T, \tag{2.1c}$$

where $(x, t) = (x, y, t)$ represents the spatial and time coordinates, $\mathbf{u} = (u, v)$ the velocity vector, ρ_0 the reference density, p the pressure, ν the kinematic viscosity, $\mathbf{g} = (g_x, 0)$ the gravity, β the thermal expansion coefficient, T the temperature, k the thermal conductivity and c the specific heat capacity. The mathematical symbols of $\nabla \cdot$, ∇ and Δ are, respectively, the divergence, gradient and Laplace operators in the particular coordinate system being used. The Boussinesq approximation is justified if $\delta\rho = \beta\delta T = \beta(T - T_c) \ll 0.1$ (Chang & Sa 1990), which is satisfied for all cases in the present study.

For the current flow configuration, the no-slip zero velocity and constant hot temperature (T_h) boundary conditions are applied to the rigid surfaces of the cylinders. The shear-free and adiabatic conditions are applied to the vertical channel walls. The coolant with temperature $T_c < T_h$ flows from the inlet face of the channel with a uniform velocity $(U_\infty, 0)$. The outlet face of the channel is assumed to be an open boundary with zero velocity and temperature gradients. The pressure is prescribed to be zero at the outlet and zero gradients at the other boundaries.

Using the variables

$$\mathbf{u}^* = \frac{\mathbf{u}}{U_\infty}, \quad x^* = \frac{x}{D}, \quad y^* = \frac{y}{D}, \quad t^* = \frac{tU_\infty}{D}, \quad p^* = \frac{p}{\rho U_\infty^2}, \quad T^* = \frac{T - T_c}{T_h - T_c}, \quad (2.2a-f)$$

equations (2.1) can be expressed in dimensionless forms as

$$\nabla \cdot \mathbf{u}^* = 0, \quad (2.3a)$$

$$\frac{\partial u^*}{\partial t^*} + \mathbf{u}^* \cdot \nabla u^* = -\nabla P^* + \frac{1}{Re} \Delta u^* + Ri \theta, \quad (2.3b)$$

$$\frac{\partial v^*}{\partial t^*} + \mathbf{u}^* \cdot \nabla v^* = -\nabla P^* + \frac{1}{Re} \Delta v^*, \quad (2.3c)$$

$$\frac{\partial \theta}{\partial t^*} + \mathbf{u}^* \cdot \nabla \theta = \frac{1}{RePr} \Delta \theta. \quad (2.3d)$$

The superscript * of the non-dimensional variables is omitted for simplicity for the rest of the paper. Equations (2.3) show that the governing parameters are *Ri*, *Re* and *Pr*, which are defined as

$$Re = \frac{U_\infty D}{\nu}, \quad Ri = \frac{g\beta(T_h - T_c)D}{U_\infty^2}, \quad Pr = \frac{\mu c}{k}, \quad (2.4a-c)$$

respectively. In the present study, the investigated range of *Ri* is from 0 to 1 to observe the gradual variation of behaviours with increasing buoyancy from forced convection. The upper limit of *Ri* = 1 is used because it can present large effects of buoyancy for flow around a solid cylinder (Hu & Koochesfahani 2011). Here *Re* is fixed at 100 since it is a typical value for laminar flow around a solid cylinder with vortex shedding; *Pr* is fixed at 7 for water.

Due to the unsteady nature of the velocity and temperature fields, it is useful to analyse the mean flow and heat transfer characteristics. The time averaged, fluctuating and root mean square (r.m.s.) of the variable ψ are defined as

$$\bar{\psi} = \frac{1}{t_2^* - t_1^*} \int_{t_1^*}^{t_2^*} \psi \, dt, \quad \psi' = \psi - \bar{\psi}, \quad \psi'_{rms} = \sqrt{\frac{1}{t_2^* - t_1^*} \int_{t_1^*}^{t_2^*} (\psi - \bar{\psi})^2 \, dt}, \quad (2.5a-c)$$

respectively. The $(t_2^* - t_1^*)$ is the time duration of the flow in the saturated (fully developed) state. For flow within the array, the Eulerian-averaged variable is calculated as

$$\langle \bar{\psi} \rangle = \frac{1}{V_a(1 - \phi)} \int_{V_a(1 - \phi)} \bar{\psi} \, dV, \quad (2.6)$$

where V_a is the volume/cross-sectional area of any arbitrary representative area of the array.

For force analyses, the total drag and lift coefficients (C_D and C_L) of the array are calculated from the sum of the forces exerted on the individual circular cylinder as

$$C_D = \frac{\sum_{i,j=1}^N F_{ij} \cdot \hat{x}}{1/2\rho U_\infty^2 D}, \quad C_L = \frac{\sum_{i,j=1}^N F_{ij} \cdot \hat{y}}{1/2\rho U_\infty^2 D}, \quad (2.7a,b)$$

where i, j are the labels of each cylinder in the x and y directions, respectively; \hat{x} and \hat{y} are the unit vector in the horizontal and vertical directions, respectively. The force on the

cylinder (i, j) is expressed as $F_{ij} = \int_{S_{c,ij}} (p\mathbf{I} - \boldsymbol{\tau}) \cdot \hat{\mathbf{n}} dS_c$, where $\boldsymbol{\tau}$ is the stress tensor, \mathbf{I} the identity matrix, $S_{c,ij}$ the surface of the cylinder (i, j) and $\hat{\mathbf{n}}$ the unit surface normal vector of the cylinder. Both C_D and C_L can be decomposed into the pressure and viscous force contributions. The drag coefficient of an individual cylinder is calculated as $C_{dij} = F_{ij} \cdot \hat{\mathbf{x}}$. The mean drag coefficient of an individual cylinder ($\overline{C_{dij}}$), the mean drag coefficient of the array ($\overline{C_D}$) and the r.m.s. lift coefficient ($C_{L'rms}$) for the array are calculated from (2.5a-c). The Strouhal number (St) is calculated as fD/U_∞ with f the frequency of the global fluctuating flow including the vortex shedding behind the array.

For heat transfer analyses, the Nusselt number of the array is calculated from the sum of the local Nusselt number of an individual cylinder as

$$Nu = \sum_{i=1}^N (Nu_{dij}) = \sum_{i=1}^N \left[\int_{S_{c,ij}} \left(-\frac{\partial T^*}{\partial n} \right) dS_c \right], \tag{2.8}$$

where $\partial/\partial n$ is the gradient in the direction normal to the surface. The local Nusselt number (Nu_d) is calculated from $-(\partial T^*/\partial n)$, which is derived from the equation $k\partial T/\partial n = h(T_h - T_c)$ with h being the local heat transfer coefficient. The mean local Nusselt number ($\overline{Nu_d}$), the mean Nusselt number of an individual cylinder ($\overline{Nu_{dij}}$) and the mean Nusselt number of the array (\overline{Nu}) are calculated from (2.5a-c).

In the present study, the pressure implicit with splitting of operators scheme (Issa 1986) is used to treat the pressure-velocity coupling in the numerical framework of the finite-volume method. The convection and diffusion terms in both momentum and energy equations are discretized by the second-order upwind method. The time derivative is discretized by a second-order method. All calculations are carried out in parallel with the message passing interface method. Verification and validation tests are performed for both an individual circular cylinder and an array of cylinders (including $\phi = 1$), the details of which are presented in the Appendix section.

3. Numerical results

The numerical results are obtained for flow in the recurrent or stationary stage. A recurrent behaviour in a dynamical system characterizes the fact that the system will repeatedly (recurrently) return to any, and all, states of a stationary configuration with an infinity of such occurrences (Frisch & Kolmogorov 1995). Here, the required physical time to reach the recurrent stage largely increases with an increment in Ri and/or a decrement in ϕ .

3.1. The mean recirculation regions

The recirculation behaviours are more complicated than those of the previous studies (e.g. Sharma & Eswaran 2004; Hu & Koochesfahani 2011) on opposing-buoyancy mixed convection around a solid cylinder due to the geometrical effects of cylinder arrays. Based on the existence of different types of mean recirculation, six flow patterns (from P-1 to P-6) are identified, as indicated in figure 2.

Pattern P-1 represents symmetric flow with one vortex pair in the near wake. A typical case of P-1 is shown in figure 3(a,g,m). A region with negative velocity is shown behind the rear of the array, indicating the existence of the alternating vortex with a similar size to that of the region. Figure 2(a) shows that, for $Ri = 0$, all cases with different geometric configurations present the P-1 pattern. As Ri increases, the symmetry only remains for

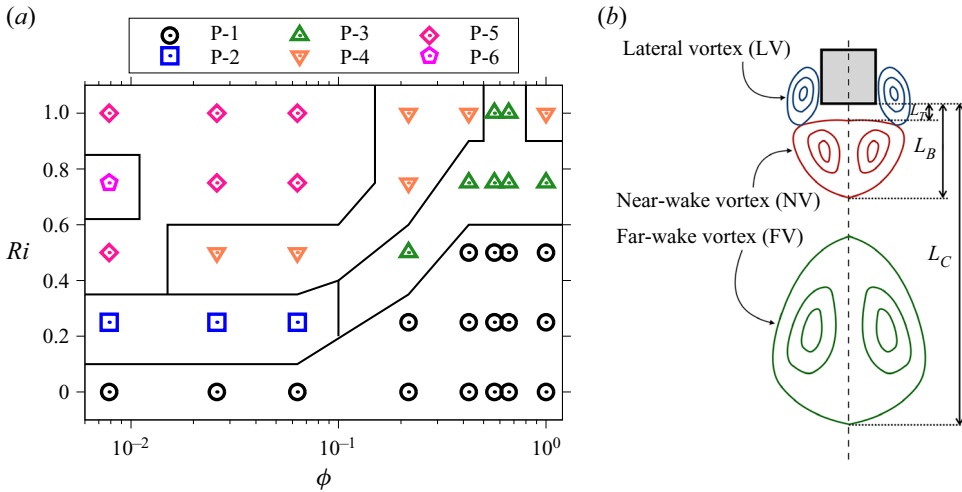


Figure 2. (a) Flow patterns based on mean recirculation regions in the parameter space of Ri and ϕ : P-1 represents symmetric flow (SF) with near-wake vortices (NV); P-2 represents unsymmetric flow (UF) with NV; P-3 represents UF with NV and lateral vortices (LV); P-4 represents UF with NV, LV, and detached far-wake vortices (FV); P-5 represents UF with NV, LV and connected FV; P-6 represents UF with NV, LV, connected FV, and a small vortex pair between LV and NV. (b) Sketch of P-4.

larger ϕ cases, which indicates that the wake flow is less affected by the buoyancy force for larger ϕ .

The corresponding temperature contours are presented in figure 4(a,g). The heat is carried away from the array via hot ‘blobs’ shedding from the two sides of the array, demonstrating ‘Kármán’ vortical structures. When the inertial flow penetrates into the array, the fluid is slowed down due to the blockage effect of the cylinders and part of it is redirected out the array from the lateral sides. If $Ri > 0$, the upward buoyancy-induced flow further slows down the inertial flow and more fluid bleeds from the lateral sides. Note that the fluid is heated up when it moves in the array. Meanwhile, the surrounding flow is also heated up when it moves along the heated ‘porous wall’. The heated lateral bleeding flow, together with the heated surrounding flow, forms the thermal layer (TL) on the lateral sides of the array. In figure 4(g) the heat is almost locked by the compact cylinders within the array and the TLs develop along the lateral sides of the array, similar to that of a solid square cylinder.

Pattern P-2 indicates the onset of unsymmetrical flows. Specifically, P-2 presents an unsymmetrical flow with one vortex pair, as shown in figure 3(h,n), which only appears when both ϕ and Ri are small. The P-2 pattern indicates that the flow in the far wake begins to be disturbed due to the pore effects even though the buoyancy is small. The wake behind the array becomes wider with decreasing ϕ . The widened wake is accompanied by more intense fluctuations further downstream, as demonstrated by the more curved streamlines. The streamlines in the far wake deviate from symmetry, where a region with almost zero velocity appears. Part of the fluid bleeds from the rear of the array, which is called the base bleed. The near-wake vortex pair is detached from the rear of the array due to the base bleed. The wake length becomes shorter, indicating that the alternating vortex rolls closer to the cylinder.

For P-2 (figure 4b), more heat is transported downstream compared with P-1 (figure 4a), indicating a larger overall heat transfer rate. The alternating shedding of hot ‘blobs’ also spans a wider space in the far wake, which contributes to the flow with more

Opposing-buoyancy mixed convection through cylinder arrays

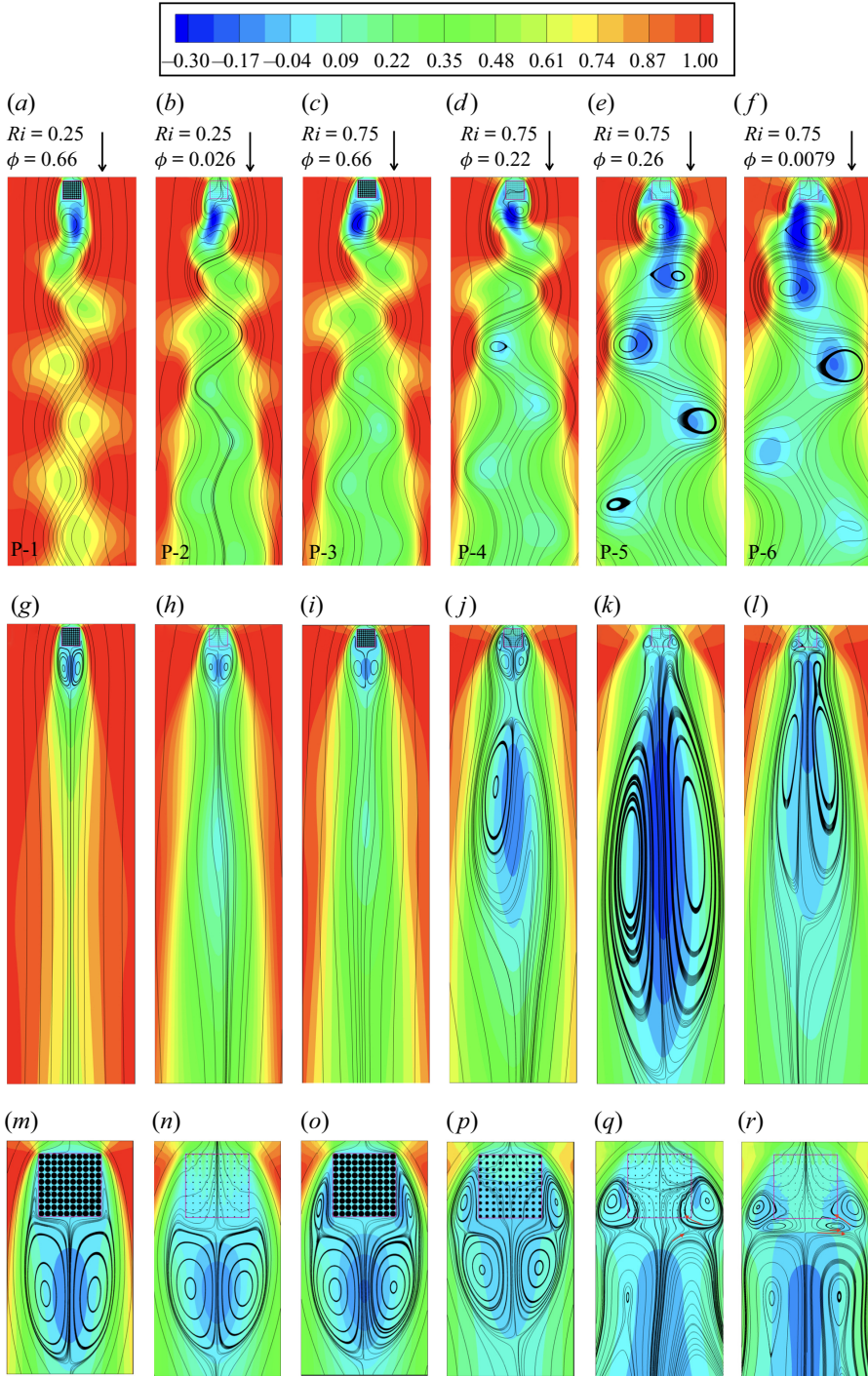


Figure 3. Plots of u -component velocity contours and streamlines for the (a–f) instantaneous flow field, (g–l) time-averaged flow field and (m–r) the near-wake region. Left to right: representative cases for patterns 1–6. The arrows in (q) and (r) indicate the local mean flow direction.

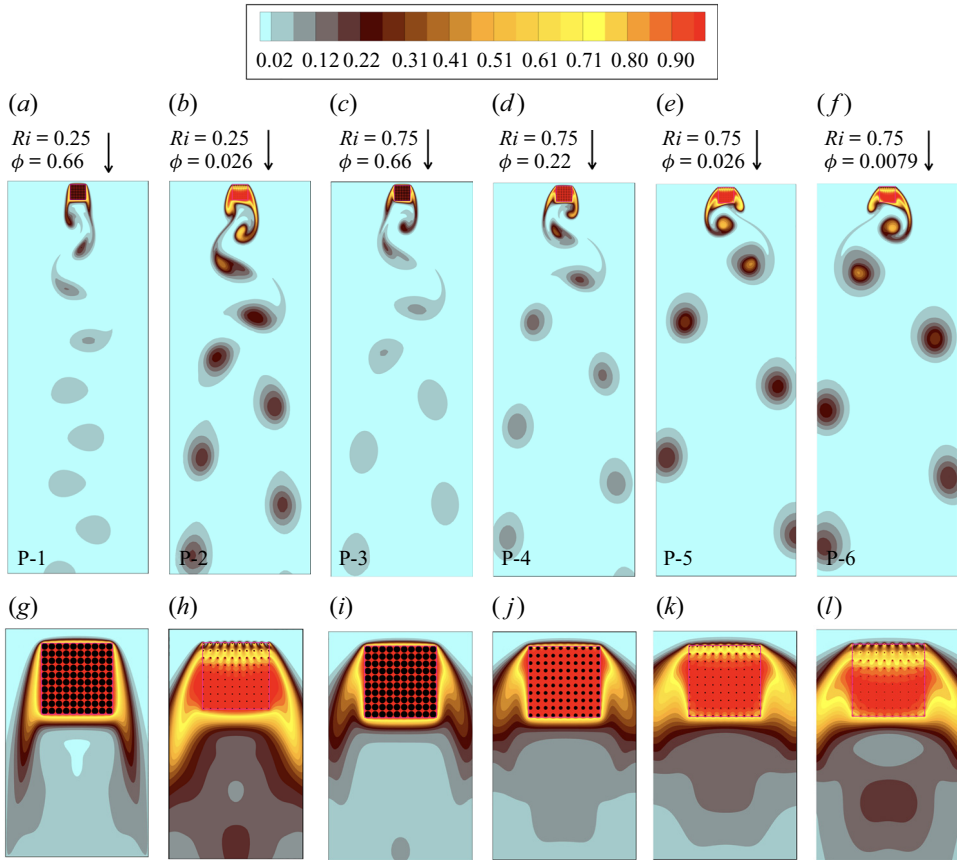


Figure 4. Temperature contours for the (a–f) instantaneous flow and (g–l) time-averaged flow in the near-wake regions. Left to right: representative cases for patterns 1–6.

intense fluctuations. Figure 4(h) shows that the inertial flow promotes heat transfer in the upstream side of the array. A fairly large amount of heat is still locked in the array because of the blockage of cylinders and the buoyancy. The TLs on the lateral sides are much thicker than those of P-1 due to the enhanced interaction between the inertial flow and the buoyancy-induced reverse flow. The fluid, which is squeezed out from the lateral sides, seems to increase the effective frontal area of the bluff body. This expanded effective frontal area sheds light on the wider wake flow and lower shedding frequency.

Pattern P-3, as shown in figure 3(i,o), also indicates the onset of unsymmetrical flows when both ϕ and Ri are relatively large. The lateral vortex pair is formed due to the relatively stronger reverse flow driven by upward buoyancy at larger Ri . Different from P-2, the asymmetry of P-3 is mainly caused by a large buoyancy force. For relatively large $Ri = 0.75$ and $\phi = 0.66$, the flow slightly deviates from symmetry with one vortex pair in the near wake, similar to that shown in figure 3(h). Patterns P-2 and P-3 indicate that the unsymmetrical region with almost zero velocity in the far wake can be caused by either large opposing buoyancy or porous effects. For relatively large $Ri = 0.75$, an additional vortex pair appears on the lateral sides of the array due to stronger buoyancy-induced reverse flow. Besides, the similar flow patterns shown in figure 3(b,c) indicate that either a larger Ri or a smaller ϕ gives rise to a wider wake.

At $Ri = 0.75$, the shedding pattern of a compact array (figure 4c) is fairly similar to that of figure 4(b) except that the temperature of vortices in figure 4(c) is much lower, implying a smaller heat transfer rate from the array. This also corresponds to a similar streamline pattern but somewhat less unsymmetric flow for $\phi = 0.66$ (figure 3i) compared with figure 3(h). Based on the heat transported downstream, the heat transfer rates indicated in figure 4(a,c) are expected to be similar. Note that P-2 and P-3 form a qualitative bifurcation region dividing the symmetric and strongly unsymmetrical flows. The corresponding Ri of the bifurcation region increases with ϕ . Comparing P-1 and P-3, the larger buoyancy promotes a stronger reversed flow on the lateral sides of the array, forming the lateral vortex that thickens the TLs and prevents the heat from transferring downstream to some extent. Comparing P-2 and P-3, the alternating vortices shedding from the array have similar width, but less heat is transferred downstream for P-3 since the lateral squeezing fluid is hindered by the higher resistance of the dense array in P-3.

Pattern P-4 represents an unsymmetrical flow with two vortex pairs and a detached recirculation region further downstream, a typical case of which is demonstrated in figure 3(d,j,p). The P-4 pattern also appears at $\phi = 1$ and $Ri = 1$ for a solid square cylinder (figure 2a). The discontinuity from a very compact array to the solid square cylinder results from the difference between the shape of the two bodies, which was also observed in the previous study (Tang *et al.* 2020, 2019). Similarly, at fixed $Ri = 0.75$ (figure 3c–f) the streamlines become more curved and the wake becomes increasingly wide as ϕ decreases from 0.66 to 0.0079. The instantaneous velocity contours show that the near-wake negative velocity region of P-4 is shorter compared with P-3; also, a small vortex begins to appear in the far wake. Figure 3(o,p) also shows that the near-wake mean closure length decreases as ϕ decreases. The temperature contours of P-4 in figure 4(d) show a wider distance between alternating shedding vortices and a higher temperature of the hot ‘blobs’ compared with P-3. The TLs are thicker owing to more heated flow exiting the array from the lateral sides.

We note that the present results are consistent with the previous experimental results. For a solid circular cylinder under opposing buoyancy at relatively large $Ri \geq 0.72$, the experiments of Hu & Koochesfahani (2011) showed that small ‘Kelvin–Helmholtz’ (KH) vortices concurrently shed in the near wake of the heated cylinder, which would merge to form larger vortex structures further downstream. Here, the small vortices are not observed, instead, the large vortex sheds alternately at the two lateral sides of the heated square cylinder or cylinder array for all Ri . This is because the flow shown here is in the recurrent stage, and the experimental results (Hu & Koochesfahani 2011) are obtained at an earlier stage of the flow evolution, showing KH instability. Although the KH vortices are not apparent in the recurrent stage, the instability indicated in the early stage of the evolution should be the same instability that causes the fluctuating velocity downstream, as will be discussed later for figure 7. As ϕ decreases, this instability increases and, therefore, results in a larger velocity deficit in the far wake.

Pattern P-5 is an unsymmetrical flow with connected near-wake and far-wake vortices, which occurs at small ϕ under large Ri , as observed in figure 3(e,k,q). The superposition of pore effects and buoyancy gives rise to a more disturbed flow. The instantaneous streamlines (figure 3e) show that the near-wake negative velocity region is much larger than that of a larger ϕ case. An enlarged vortex is closely attached to the rear of the near-wake vortex with a different rotating direction. Also, the size and number of the vortices in the far wake increase due to more complex flow interactions. The time-averaged streamlines (figure 3k) show that the near-wake vortices are ‘engulfed’ into the large recirculation downstream. It is clearly seen in the near wake (figure 3q) that the lateral vortices penetrate the more sparse array.

Figure 4(e,k) presents the corresponding temperature contours for P-5. The width of the vortex shedding is evidently larger and the frequency of vortex shedding is smaller than those of patterns 1–4, consistent with the instantaneous velocity contours shown in figure 3. The mechanism of this phenomenon lies in the interaction of buoyancy-induced flow and inertial flow. With a smaller ϕ , the permeability of the array is larger. Thus, the downward inertial flow and the upward buoyancy-induced flow can easily penetrate the array and squeeze more hot flow out of the lateral sides, forming thicker TLs. The thickened TLs expand the effective frontal area, which causes the decrease of the shedding frequency and enlargement of the width of the wake.

Pattern P-6 is similar to P-5 except that another vortex pair appears between the lateral and the near-wake vortices, as seen in figure 3(l,r). The small vortex pair is mainly caused by the compromise between the bleeding flow from the array and the much larger surrounding (lateral and the near-wake) vortices. Similar small vortices were also observed by Sharma & Eswaran (2004) at $Ri = 0.5$ and $Pr = 0.7$, which are attached to the rear side of the array due to the interaction of the buoyancy-induced flow and the vortices behind the cylinder. The size of the connected near-wake and far-wake vortices becomes smaller than that presented in figure 3(k) due to the smaller strength of the fluctuation in the far wake, as will be discussed for figure 7. The temperature contours in figure 4(f,l) show that more heat is convected downwards for P-6. For relatively small ϕ , the frequency of vortex shedding at higher Ri is smaller.

Note that patterns of P-4, P-5, P-6 on the upper side of the bifurcation region all present large recirculation further downstream, showing strong unsymmetrical behaviours. The interaction of the inertial flow and the buoyancy-induced reverse flow occurs within the array as well as on the lateral surfaces of the array. The interaction inside the array squeezes the fluid toward the lateral sides and thickens the TLs. The interaction on the lateral surfaces induces instability of the squeezed flow, which is transported downstream, forming detached vortices. The lateral bleeding flow becomes stronger with increasing Ri and decreasing ϕ . Meanwhile, the heat transfer rate from the bottom row of the cylinder array increases, also due to the enhanced buoyancy-induced reverse flow with increasing Ri and decreasing ϕ .

Figure 2(b) shows a sketch of the typical averaged flow structure, using P-4 as an example. Here L_B is the distance between the rear of the array and the rear stagnation point of the near-wake vortices; L_C is the distance between the rear side and the farthest stagnation point on the centreline no matter if the near wake is connected with the far wake or not. For cases without vortices in the far wake, L_C is taken to be the same as L_B . The distance between the rear of the array and the first saddle point in the centreline is denoted as L_T .

The flow structure is mainly determined by the interaction among the inertial flow, the buoyancy-induced reverse flow and the cylinder array. If the buoyancy-induced reverse flow and the block effect of the cylinder array are weak, part of the inertial flow passes through the array and then reaches a stagnation point downstream of the array. However, this stagnation point may be located within the array when ϕ and Ri are relatively large. Thus, the penetration depth $L_P = D + L_T$, which reflects the location of the stagnation point, can be defined to quantitatively describe this interaction. The penetration depth is largely dependent on the strength of the penetrating inertial flow and the buoyancy-induced reverse flow at various Ri and ϕ . The tendency of variation of penetration depth with Ri is similar to that shown by Goldman & Jaluria (1986) for negatively buoyant flows.

Figure 5 shows the summary of the length of the vortex in the centreline. As shown in figure 5(a), L_C can be very large for relatively high Ri and/or low ϕ . For the solid square

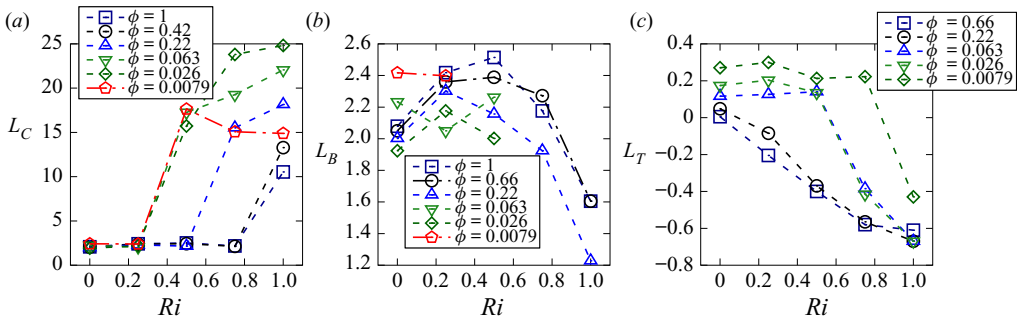


Figure 5. Variations of (a) L_C , (b) L_B and (c) L_T with Ri for different ϕ .

cylinder, L_C first decreases slightly and then increases to around $10.5D$, the tendency of which is consistent with the previous experimental results (Hu & Koochesfahani 2011) for a solid circular cylinder. The L_C at $\phi = 0.42$ is fairly similar to that of the solid case, as indicated earlier in figure 2. It is observed that the L_C at $Ri = 1$ increases as ϕ decreases from 0.22 to 0.026. However, the L_C at $Ri = 1$ decreases when ϕ further decreases to 0.0079. The largest L_C is $\sim 25D$ for $\phi = 0.026$ and $Ri = 1$, which is more than twice as large as that of flow around a solid counterpart.

Figure 5(b) shows the variation of L_B with Ri . For $\phi \geq 0.22$, L_B first increases and then decreases with Ri . The decreasing trend is consistent with that of Sharma & Eswaran (2004). The L_B at $\phi = 0.66$ is quite similar to that of the solid case, while the L_B at $\phi = 0.22$ is evidently smaller than those of the compact array cases. For small $\phi \leq 0.063$, L_B is obtained only at relatively small Ri when the near-wake and far-wake vortexes are separated. The L_B at $\phi = 0.026$ follows the trend of the larger ϕ cases though it is noticeably smaller. Unexpectedly, the variation trend of L_B at $\phi = 0.063$ is opposite to those at $\phi \geq 0.22$, but is consistent with that of $\phi = 0.0079$. This is actually due to the balanced effects of the base bleed and the fluctuating intensity of the flow since the base bleed distance is included in L_B . For $\phi = 0.063$ and 0.0079, the base bleed is much larger than those of the compact array cases, resulting in larger L_B . For $\phi = 0.026$, although the base bleed is also large, the mean vortex is much shorter due to the faster shedding of vortexes. Overall, L_B for small ϕ does not vary much with Ri , which ranges from approximately 2 to 2.4.

Figure 5(c) shows the variation of L_T with Ri . For large $\phi = 0.66$, the magnitude of L_T increases monotonically with Ri and L_P decreases correspondingly since the buoyancy force is comparably larger than the inertial flow within the compact array. For $\phi = 0.22$, L_T slightly deviates from those of larger ϕ cases. The L_T at $\phi \leq 0.063$ is positive for small Ri since the array allows more inertial flow to go through it; L_T is negative at larger Ri since the reverse flow becomes strong, which penetrates through the array from the bottom.

Figure 6 shows a summary of the length of the lateral vortex pair, which is mainly formed by the interaction of upward buoyancy and downward inertial flow. In the present work, the lateral vortex pair only occurs for $Ri \geq 0.5$. This indicates that the large reverse flow induced by buoyancy is the main factor promoting the formation of the lateral vortexes. Also, the lateral vortex pair occurs at a smaller Ri when ϕ is smaller, demonstrating that a certain pore structure of the array can promote the formation of the lateral vortexes. Figure 6 demonstrates variations of the relative positions of the lateral vortex core (C_X, C_Y) and the saddle point (S_X, S_Y) with ϕ at different Ri . Figure 6(a) shows that the absolute values of C_Y increase with Ri , indicating that the vortex core moves

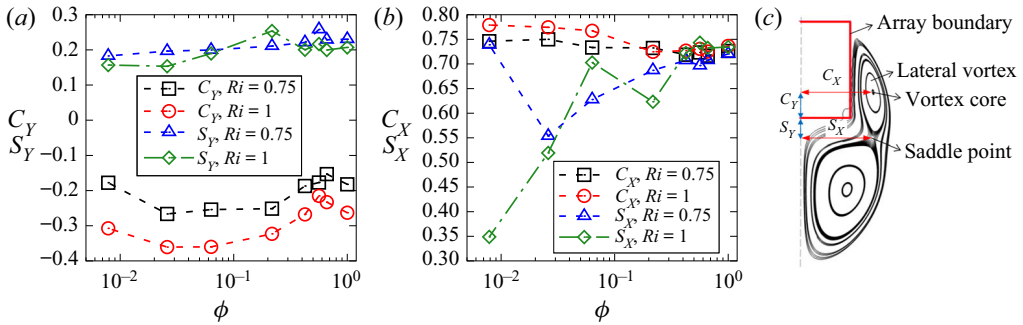


Figure 6. Variations of (a) C_Y, S_Y and (b) C_X, S_X with ϕ . (c) Illustration of the lateral and near-wake vortices.

upward along with increasing buoyancy. For fixed Ri , C_Y first decreases, then increases and finally decreases with an increment of ϕ , which is due to the competence of the inertial flow and the buoyancy-induced flow under porous effects. On the other hand, S_Y does not change much across the range of ϕ for different Ri , which is ~ 0.2 .

Contrastingly, figure 6(b) shows that C_X does not change much with ϕ and Ri , which is approximately 0.75, while S_X differs much with both parameters, especially at small ϕ . The variation of S_X with ϕ shows a fluctuating trend due to the more complicated wake behaviours, e.g. the appearance of an additional vortex pair between the lateral and near-wake vortices. Overall, S_X at smaller ϕ is shorter, which implies that the vortex size is larger. In addition, the lateral vortices are largely related to the TLs on the two sides of the array, as demonstrated by the mean temperature in figure 4. The forced inertial flow develops a downward viscous layer on the array surface, which comes across the upward viscous layer formed by the buoyancy-induced reverse flow, resulting in an enclosed zone with heat kept inside and a recirculation formed beneath it. The enclosed zone is wider for smaller ϕ because of the lateral bleeding of the heated flow.

We next present more analyses on the transition behaviours between different flow patterns. The transition between P-1 and P-2 mainly occurs at relatively small $0.0079 < \phi < 0.1$ and $0 < Ri < 0.25$ since the evident upward buoyancy within the array causes a small instability in the far wake. For relatively large $0.1 < \phi < 1$ and $0.25 < Ri < 0.5$, the flow pattern transits from P-1 to P-3 due to the buoyancy-induced flow separation on the lateral sides of the array. The transition from P-3 to P-4 occurs at relatively large $0.1 < \phi < 0.56$ and $0.5 < Ri \leq 1$ since the instability in the far wake increases, forming vortices, with increasing buoyancy effects. The flow can also transit directly from P-2 to P-4 at $0.026 < \phi < 0.1$ and $0.25 < Ri < 0.5$, indicating that a porous medium promotes instability even at moderate buoyancy force. The flow transits from P-4 to P-5 at $0.026 < \phi < 0.1$ and $0.5 < Ri \leq 1$ because the area with strong instability further increases in the far wake, causing connection of the near- and far-wake vortices. Note that at $\phi = 0.0079$, P-2 directly transits to P-5 due to the large pore effects on the instability downstream. The mechanism that leads to the far wake is related to the fluctuations. The fluctuations are caused by the instability triggered by the upward buoyancy-induced reverse flow and the downward inertial flow. With the increments of the countercurrent flow, more unsteady structures are formulated on the lateral surfaces, which move downstream and form larger detached vortices behind the array.

As indicated above, the fluctuations caused by the instability play an important role in the far-wake behaviour. Therefore, a detailed discussion on the instability indicated by the

Opposing-buoyancy mixed convection through cylinder arrays

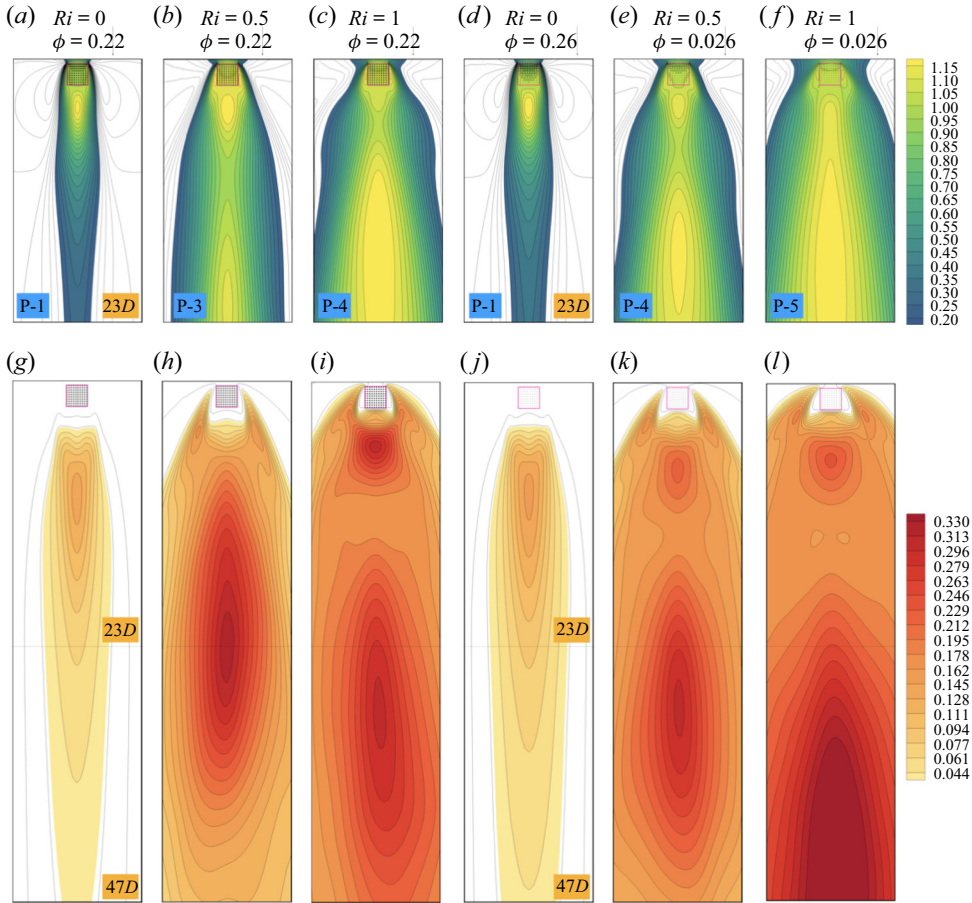


Figure 7. Distributions of the mean velocity deficit (MVD) (a–f) and the fluctuating kinetic energy (FKE) (g–l) for different Ri and ϕ as indicated.

fluctuating kinetic energy (FKE) and the fluctuating heat flux (FHF) is provided below. Here, FKE is calculated from $0.5 \times [(u'_{rms})^2 + (v'_{rms})^2]$. Figure 7 shows distributions of mean velocity deficit (MVD) (a–f) and FKE (g–l) at various Ri and ϕ . Here, MVD is calculated as $(U_\infty - \bar{u})/U_\infty$. The flow pattern based on figure 2 is indicated on the left corner of each MVD figure. The distance between the rear of the array and the bottom boundary of the figure is $23D$ and $47D$ for MVD and FKE, respectively.

For relatively large $\phi = 0.22$ (figure 7a–c,g–i), the region with $MVD \geq 0.2$ becomes larger with an increment in Ri . Correspondingly, the region with $FKE \geq 0.044$ also enlarges evidently with increasing Ri . At $Ri = 0$ (figure 7a,g), the region with high MVD values mainly exists right behind the rear of the array, where a vortex pair is formed. It is seen that FKE in the region of the near-wake vortex is very small. The largest FKE appears behind the vortex region. At $Ri = 0.5$ (figure 7b,h), two local maximums of MVD appear at the near-wake and far-wake regions, respectively, though no vortex is actually formed in the far wake (P-3 pattern). The FKE in the region of the near-wake vortex is also very small, which increases and reaches a local maximum at approximately $23D$ downstream of the array. The local maximums of MVD and FKE appear in roughly the same area. At $Ri = 1$ (figure 7c,i), the local maximums of MVD move further upstream.

The distance between the local maximums is also smaller. Pattern P-4 indicates that the large recirculation is formed in the far wake, which is detached from the near-wake vortex. In this case, a local maximum of FKE occurs in the region between the near- and far-wake vortexes, indicating that the locally strongest fluctuation occurs when the flanks of the two contra-rotating vortexes clash with each other. Also, a local maximum of FKE appears further downstream due to the energy cascade from the detached vortexes.

For relatively small ϕ (figure 7*d-f,j-l*), the region with large MVD is evidently larger, especially for mixed convection. The fluctuations are also much more intense, especially for $Ri = 1$. The local maximum of FKE also moves further downstream for smaller ϕ . Overall, the large recirculation zone in the far wake is well correlated with FKE. For moderate fluctuating intensity, the recirculation region is detached from the near-wake vortex. As FKE increases, the recirculation region becomes larger. Once the recirculation enlarges to a certain size, it comes across the near-wake vortex and connects as well as develops with it. This also indicates that the formation mechanisms of the near-wake and far-wake vortexes are different. The near-wake vortex mainly results from flow separation from the extended shear layer formed by the bleeding flow from the rear of the array and the surrounding fluid flow on the lateral sides of the array, while the far-wake vortexes are somewhat related to the fluctuations from the instabilities developed from the interaction of the opposing buoyancy with the inertial flow, which is intensified by the porous matrix of the array.

The variations of MVD and FKE with the streamwise distance along the centreline are also presented in figure 8. The region with MVD greater than 1 indicates the formation of vortexes. Figure 8(*a*) shows that, under forced convection, MVDs are almost the same for all the presented cases for $x/D \leq 3$, which is the length of the near-wake vortex. The decreasing rate of $\phi = 0.0079$ is relatively small. Correspondingly, FKE is larger as ϕ decreases though FKE does not differ much among all ϕ cases.

As Ri increases to 0.5 (figure 8*b*), the difference among various ϕ is obvious. For $\phi = 0.66$, MVD is similar to that of forced convection except that MVD in the far wake is still much larger than that of $Ri = 0$. The maximum value of FKE occurs at approximately $x/D = 9$. For $\phi = 0.22$, a secondary velocity deficit (bump) occurs at $x/D \sim 11$, but the vortex is not literally formed since the maximum value of the second bump is ~ 1 . The variation trend of the corresponding FKE is also similar to that under forced convection but the value of FKE is much larger. For smaller $\phi \leq 0.026$, MVD is presented with two local maximums (two bumps), both of which are noticeably larger than 1, indicating the formation of vortexes. The FKE also shows two bumps in these cases. Overall, the present results are consistent with those of the previous study (Hu & Koochesfahani 2011) since both studies indicate a large MVD region behind the body at large Ri . However, the current results show that the velocity can recover up to around 0.1 before the secondary deficit while the velocity reported by Hu & Koochesfahani (2011) is almost zero. Also, the present study shows that the velocity deficit does not always indicate a recirculation downstream. The differences partially come from the different stages of flow investigated in the two studies.

For $Ri = 1$, the decreasing rates of MVD with x/D are much smaller compared with smaller Ri cases. At $\phi = 0.66$, MVD shows two bumps with the second one below 1, therefore, no vortex appears. The FKE also only has one peak. At $\phi = 0.22$, the second velocity deficit region is much larger than the first one. The FKE shows two bumps with similar peak values. At smaller $\phi = 0.026$, the recirculation in the far wake becomes much larger. It is observed that the local maximum of FKE for the second bump is the highest among all ϕ cases, which corresponds to the smallest decreasing rate of MVD.

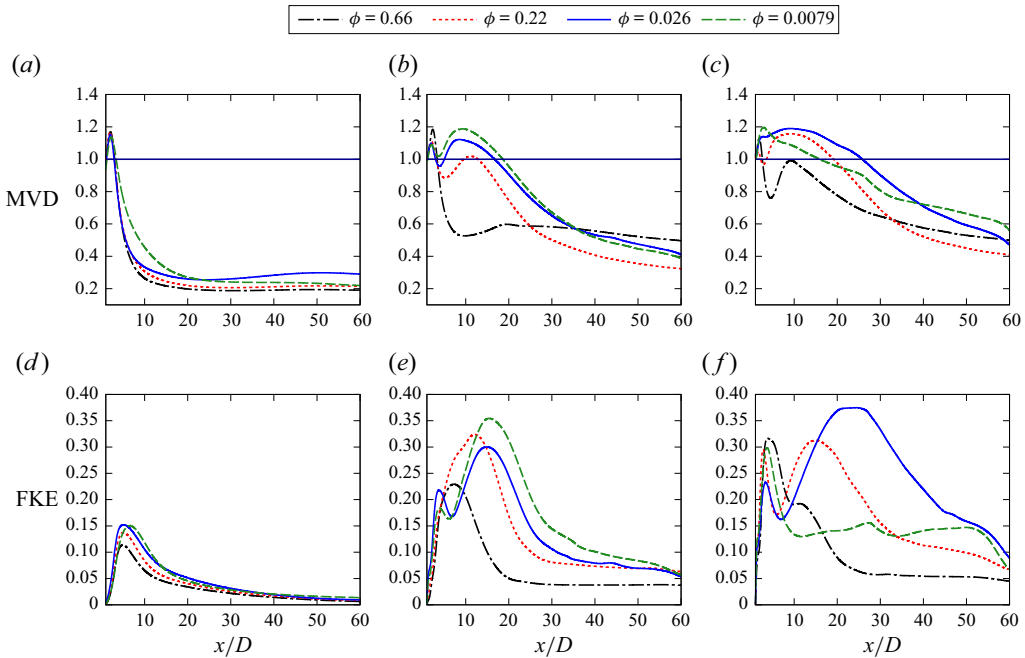


Figure 8. Variations of (a-c) MVD and (d-f) FKE with x/D for (a,d) $Ri = 0$, (b,e) $Ri = 0.5$ and (c,f) $Ri = 1$.

For $\phi = 0.0079$, both FKE and MVD are noticeably smaller than the cases of $\phi = 0.026$. Also, for $\phi = 0.026$ and 0.0079 , only one peak is shown for MVD due to the connection of the near-wake and far-wake vortices. However, FKE still shows two bumps, indicating that it is actually two types of vortices.

Apart from this, the FHF is also calculated since the intense FKE in the far wake is considered to be transported from the lateral sides of the array, where FHF is strong. The FHF is calculated as $\sqrt{\overline{(u'T')^2} + \overline{(v'T')^2}}$, where the fluctuating velocity and temperature are obtained at the same time. Figure 9 shows the distributions of FHF for various Ri and ϕ . For $\phi = 0.22$ and $Ri = 0$, two regional pairs with local maximums of FHF are shown in the near wake of the array. The smaller regional pair is on the lateral sides of the larger regional pair. As Ri increases, the regional pair on the lateral sides moves upstream and becomes much larger, while the regional pair in the middle becomes noticeably smaller. The distance between each pair of regions is also larger. The trend is more obvious at $Ri = 1$, where the local maximum of FHF in the lateral regional pair is much higher than those of smaller Ri cases. The instability caused by FHF mainly develops on the lateral sides of the array and accumulates as the fluid flows downstream. For relatively small FHF, the instability transported downstream is not sufficiently strong to form a large recirculation (figure 9b). For larger FHF, the accumulated instability promotes the formation of large recirculation in the far wake. If the accumulation takes a much longer distance than the length of the near-wake vortices, the large recirculation would be detached from the near-wake vortices, which is the situation for figure 9(c).

For relatively small $\phi = 0.026$, the distributions of FHF undergo similar changes with an increment of Ri , except that the regional pairs are much larger compared with the case of $\phi = 0.22$. Also, an additional regional pair is presented behind the array for $Ri = 0.5$ due to the pore effects of the array, which promotes the formation of detached

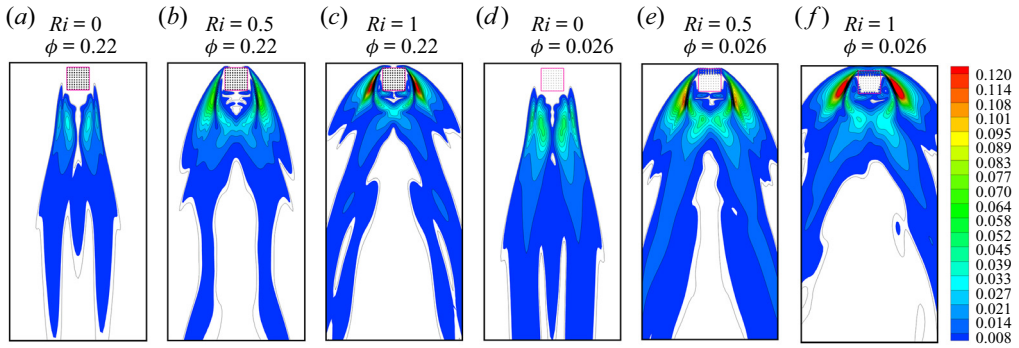


Figure 9. Distribution of FHF for different Ri and ϕ as indicated.

recirculation downstream. For $Ri = 1$, the lateral instability caused by large FHF is also large, which requires less distance for accumulation, so the large recirculation can be formed more upstream of the array. This also indicates that the large recirculation is easier to interact with the near-wake vortices within such a short distance. The analyses are also consistent with the observations made by Hu & Koochesfahani (2011), where the KH-like small vortex structures shed on the two sides of the circular cylinder, which would merge to form larger vortex structures further downstream. The merging process was found to be similar to the ‘pairing’ process of ‘KH’ vortex structures in a free shear layer. As already indicated in the last section, the phenomenon observed by Hu & Koochesfahani (2011) might be from an earlier stage of the flow. Here, although KH vortices were not observed, their effects are still accumulated and would contribute to the formation of the large recirculation further downstream.

The mean flow on the lateral sides of the array is closely related to FHF. Figure 10 shows the mean u -component velocity and the corresponding FHF profiles with respect to y/D at fixed $x = D$. The lateral surface of the array is at $y/D = 0$. For $Ri = 0$ (figure 10a,d), drastic changes of both \bar{u} and FHF occur at $y/D \lesssim 0.6$. For the presented ϕ , \bar{u} first increases to a maximum value and then decreases gradually to the free-stream velocity with y/D , similar to that of flow around a solid cylinder. For fixed y/D , \bar{u} decreases as ϕ decreases though the difference among the presented ϕ is small. In the range of $y/D \lesssim 0.6$, FHF first increases rapidly to a maximum value and then decreases sharply to zero. The maximum value of FHF as well as the range of y/D with non-zero FHF increase with decreasing ϕ . This indicates that the porous lateral surface with flow injection promotes fluctuating intensity. Overall, FHF does not have large effects on \bar{u} since FHF is relatively small with $O(10^{-3})$.

The mean u -component velocity profiles at very small Ri are also similar to those presented in figure 10(a). For these cases, the boundary layer thickness is much smaller than the side length of the array; therefore, the flow behaviour is expected to be similar to that of flow over a flat plate and the flow can be described by the simplified equations of the boundary layer flow (BLF) as

$$u \frac{\partial u}{\partial x} + v \frac{\partial u}{\partial y} = \nu \frac{\partial^2 u}{\partial y^2} - g\beta(T - T_c), \tag{3.1a}$$

$$u \frac{\partial T}{\partial x} + v \frac{\partial T}{\partial y} = \alpha \frac{\partial^2 T}{\partial y^2}, \tag{3.1b}$$

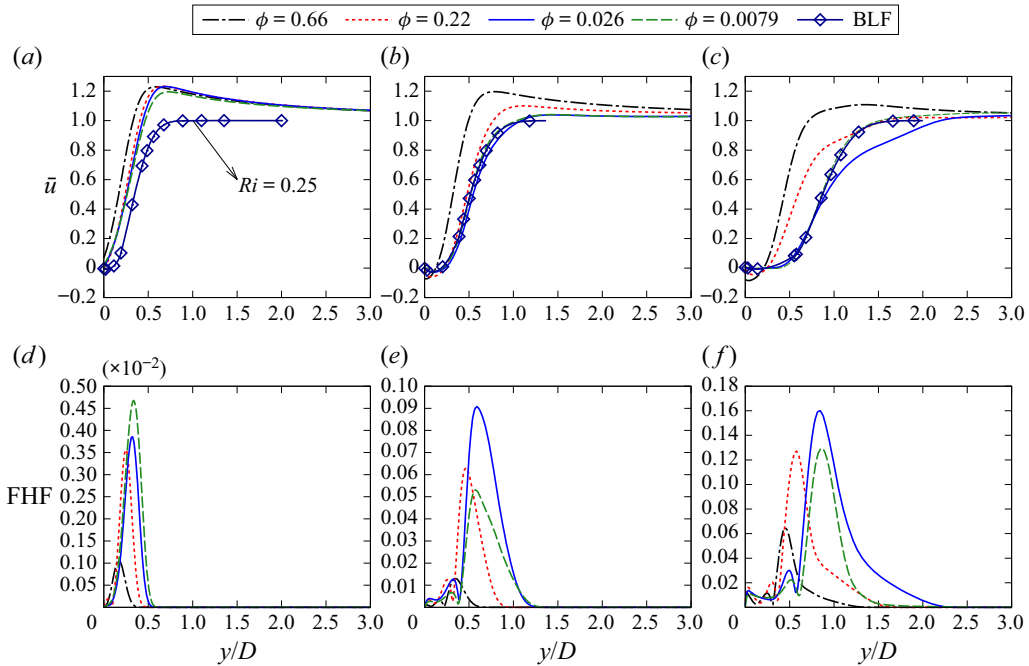


Figure 10. Variations of (a–c) the mean velocity and (d–f) the FHF with y/D at fixed $x = D$ for (a,d) $Ri = 0$, (b,e) $Ri = 0.5$ and (c,f) $Ri = 1$. The BLE solutions are obtained at $\phi = 0.0079$.

with the divergence condition. The equations were demonstrated to be applicable for forced convection as well as mixed convection with aiding buoyancy (Makinde & Olanrewaju 2010). Equations (3.1) can be transferred to the simpler ordinary differential equation (ODE) by using the similarity variable method. The coupled ODE can then be solved by using the shooting method. Preliminary calculations for forced and mixed convection with very small opposing buoyancy are performed. The BLE velocity profile at $Ri = 0.25$ and $\phi = 0.0079$ is presented in figure 10(a), which is similar to the numerical results under forced convection, except for the velocity far away from the lateral surface due to the difference between a real flat plate and a bluff body.

With the effects of larger opposing buoyancy (figure 10b,e), the differences in the \bar{u} and FHF profiles among various ϕ are much larger. In the region close to the lateral surface (inner region), \bar{u} either increases with a much smaller rate or varies non-monotonically with y/D compared with that under forced convection due to the diffusion caused by the reverse flow and the lateral vortex. The FHF in the inner region is relatively small ($\lesssim 0.01$). In the region further away from the lateral surface (outer region), \bar{u} increases drastically with y/D . The corresponding FHF also varies tremendously with y/D . It is seen that \bar{u} decreases with decreasing ϕ for $\phi \leq 0.026$, but then increases as ϕ further decreases to 0.0079. This is also reflected in figure 10(e), where the maximum FHF is observed for $\phi = 0.026$. The value of FHF also becomes much larger with opposing buoyancy. For small ϕ , the maximum \bar{u} is no greater than the free-stream velocity since part of the fluid flows through the array. The range of y/D with non-zero FHF also extends to approximately 1.5.

For even larger $Ri = 1$ (figure 10c,f), the variation trends observed at $Ri = 0.5$ are more obvious. The inner region becomes larger due to the growing size of the diffusing vortex. The corresponding FHF is also small in this region. In the outer region the maximum \bar{u} for all ϕ becomes even smaller since more fluid flows through the array, which also indicates

that the resistance of the array is smaller for larger Ri . The region with the largest variation of \bar{u} and non-zero FHF also extends to $y/D = 3$ for $\phi = 0.0079$. Overall, the enhanced buoyancy and the porous matrix intensify the fluctuations.

Obviously, (3.1) cannot be directly applied to flow with relatively large opposing buoyancy due to the formation of lateral vortexes. However, the equations still produce reasonable results if the viscosity is modified with an appropriate value. For relatively large Ri , the whole domain can be divided into the inner region close to the boundary and the outer region for the rest of the domain. The variable at the interface is assumed to be known from the direct numerical simulation. The modified viscosity (ν_e) in each region is determined from trial and error. It is seen in figure 3.1(b,c) that the BLF solutions agree well with the numerical results when ν_e is applied. For $Ri = 0.5$, $\nu_e/\nu = 8$ and 1.6 for inner and outer regions, respectively; for $Ri = 1$, $\nu_e/\nu = 70$ and 4 for inner and outer regions, respectively. In the trial and error process, ν_e is found to increase with increasing Ri and/or decreasing ϕ . Also, a more accurate estimation of ν_e is expected to follow the variation trend of FHF with y/D (see figure 10e,f), i.e. ν_e first increases and then decreases with y/D , indicating that ν_e is highly related to the fluctuations. The modified viscosity mainly adds artificial dissipation to the flow, which is quite similar to the concept of eddy viscosity in turbulence modelling.

3.2. The force coefficients

The fluctuating force coefficients exerted on the whole array are considered in this section. Figure 11 shows the representative phase portraits of C_D and C_L at $\phi = 0.0079$ and $Ri \geq 0.5$. The corresponding power spectra density (PSD) obtained from the time series of C_L is also presented. At $Ri = 0.5$ (figure 11a,d), the phase portrait presents a very narrow band of orbits similar to the limit cycles. The PSD shows a single sharp peak at $St = 0.092$, indicating that it is still a periodic (P) flow. The St for the peak amplitude depicts the frequency of vortex shedding of the near-wake vortexes. For $Ri = 0.75$ (figure 11b,e), the phase portrait becomes more complicated with wide bands of cycling orbits. The corresponding PSD also shows some noisy power spectra surrounding the peak, presenting periodic (P*) behaviours that are different from those in figure 11(a,d). The phase portrait is even more complex for $Ri = 1$ (figure 11c), presenting direct orbits from one ‘wing’ to the other. The PSD (figure 11f) shows distinctly three peaks with comparable amplitudes, which is denoted as quasi-periodic (QP).

The dynamic behaviours are closely related to the vortexes formed behind the rear side and on the lateral sides of the array. A summary of the flow behaviours is also provided in figure 12 for $Ri \geq 0.5$ and $\phi \leq 0.22$, along with the indications of flow patterns in the presented range of parameters. The dynamic behaviours for P-1, P-2 and P-3 are all periodic since the near-wake vortex shedding is the major cause of fluctuation. The behaviours in the P-4 region are also periodic because the large recirculation is detached from the near-wake vortex without influencing the dynamic behaviour of the integrated forces.

In P-5 and P-6 regions, different types of behaviours are shown. For either smaller Ri or larger ϕ , the periodic behaviours are observed because the large recirculation is only weakly connected with the near-wake vortex and, therefore, has negligible effects on the periodicity (e.g. figure 11a,d). For larger $Ri \geq 0.75$, the P* behaviour occurs (e.g. figure 11b,e). This is because the large recirculation is moderately connected with the near-wake vortex, affecting the original vortex shedding mode to some extent. For $Ri = 1$ at relatively small ϕ , behaviours of noisy subharmonic and quasi-periodic appear.

Opposing-buoyancy mixed convection through cylinder arrays

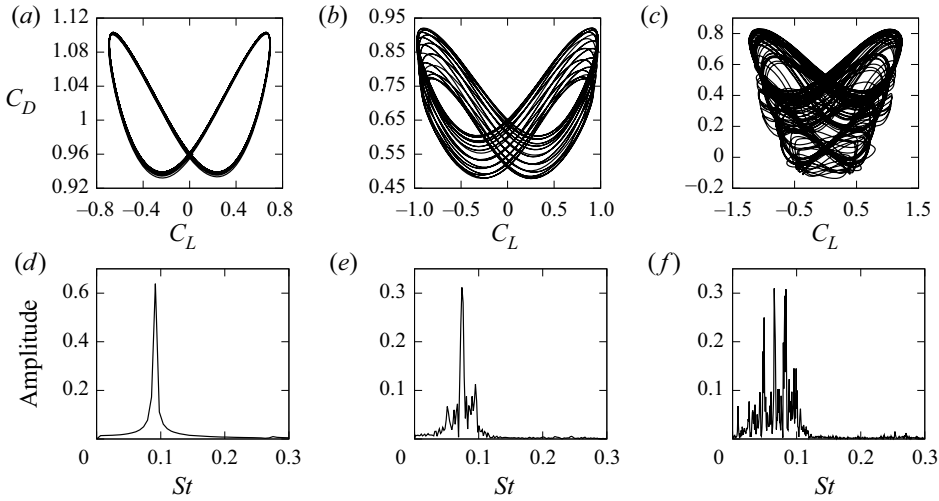


Figure 11. Phase portrait (a–c) and PSD (d–f) at fixed $\phi = 0.0079$ for (a,d) $Ri = 0.5$, (b,e) $Ri = 0.75$, (c,f) $Ri = 1$.

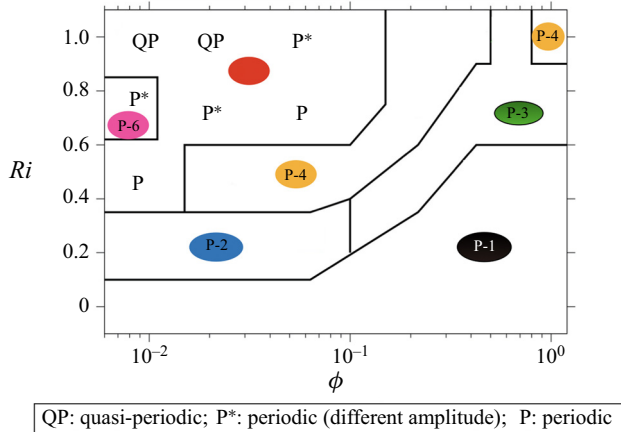


Figure 12. Power spectra density behaviours of the array-scale force coefficients, all other points are periodic.

In this circumference, the large recirculation is strongly connected with the near-wake vortices, which affects the integrated force with a different frequency. Also, large parts of the lateral vortices penetrate the array, which gives rise to a third distinct peak of the PSD. Here, the difference between quasi-periodic and noisy subharmonic is due to the relative amplitudes of the three peaks. For noisy subharmonic, the subharmonic peaks due to the large recirculation and the lateral vortices are evidently smaller than that of the fundamental peak; while for quasi-periodic, the subharmonic peaks are comparable to the fundamental peak.

As indicated above, the case with $\phi = 0.0079$ and $Ri = 1$ shows the most noisy behaviours for the investigated range of parameters. The observations also support the results and analyses in the previous study (Tang *et al.* 2020) that the critical Re for the transition from steady to unsteady flow past a cylinder array is the smallest for $\phi = 0.0079$, which is due to the interactions of inertial and viscous forces within the array.

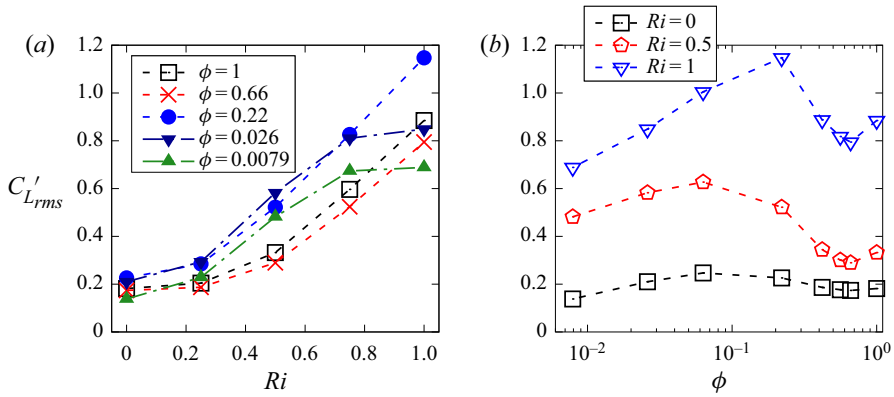


Figure 13. Variations of $C_{L'rms}'$ with (a) Ri and (b) ϕ .

Here, the opposing buoyancy intensifies the interactions of forces between cylinders, which is expected to further decrease the critical Re . Although the noisy behaviour contributes to the triggering of unsteadiness, it does not necessarily result in large fluctuations as well as the large mean recirculation in the far wake. This is consistent with the observation that the largest recirculation downstream occurs at $\phi = 0.026$ rather than $\phi = 0.0079$ (figure 5a). The large recirculation in the far wake mainly results from a combined effect of the complexity and the amplitudes of the fluctuations.

Figure 13(a) shows the variation of $C_{L'rms}'$ with Ri at different ϕ . For $\phi = 1$, $C_{L'rms}'$ increases with Ri , consistent with the previous study (Sharma & Eswaran 2004). The $C_{L'rms}'$ of $\phi = 0.66$ are noticeably smaller than that of other ϕ for the investigated range of Ri . For an array with $\phi = 0.22$, $C_{L'rms}'$ also increases monotonically with increasing Ri but with much larger values. This is because the interacting forces in the array become more active, resulting in more intense fluctuations than the solid square cylinder. For $\phi = 0.0079$, $C_{L'rms}'$ also increases with Ri , but with a trivial increment for larger Ri . The increasing rate declines when Ri is larger. The variation trends are also similar to those of $C_{L'rms}'$ with Re in the previous study (Tang *et al.* 2020). The variation trend of the fluctuation of C_D with Ri is also similar to that of C_L , thus not repeated here.

The variations of $C_{L'rms}'$ with ϕ at fixed Ri are presented in figure 13(b). For all Ri , $C_{L'rms}'$ decreases as ϕ decreases from 1 to 0.66, which implies that the compact array of circular cylinders with round corners could decline the intense fluctuations brought about by the sharp corners of the square cylinder. The discontinuity is also revealed in figure 2, where P-4 presents for both $\phi = 1$ and 0.42 while P-3 presents for both $\phi = 0.56$ and 0.66. For $\phi \leq 0.063$, $C_{L'rms}'$ decreases with decreasing ϕ , showing a peak value of $C_{L'rms}'$ in the investigated range of ϕ . This results from the changes in interacting force among the cylinders. As the distance between the cylinders becomes larger, the interaction changes from the viscous-force-dominated interaction to the inertial-force-dominated interaction, which decreases the coherent forces within the array.

The Strouhal number for the array-scale vortex shedding (St_v) is also investigated. For most cases, the flow is periodic so that the shedding frequency of vortexes is easy to detect. For certain cases with noisy behaviours (e.g. figure 11f), the frequency of the highest power is obtained. Figure 14(a) shows variations of St_v with Ri at different ϕ . For $\phi = 1$, St_v decreases monotonically with increasing Ri , the trend of which is consistent with the previous studies (Chang & Sa 1990; Sharma & Eswaran 2004; Hu & Koochesfahani 2011). It is also observed that St_v does not vary much among cases with $\phi \geq 0.22$. As ϕ

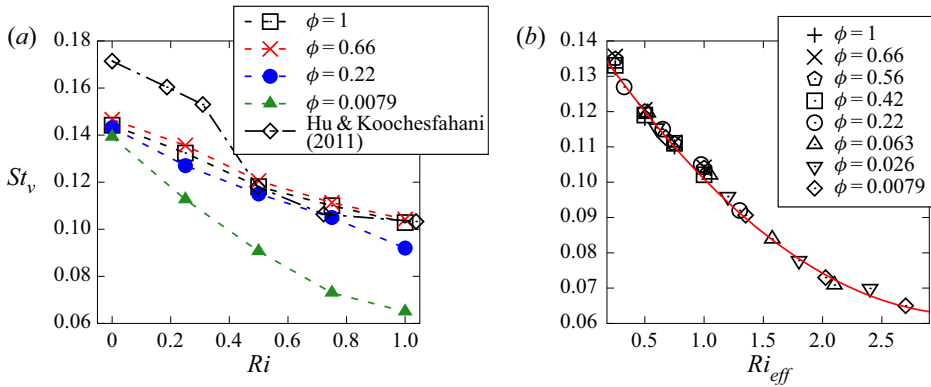


Figure 14. Plot of St_v varying with (a) Ri and (b) Ri_{eff} for different ϕ as indicated.

decreases, the decreasing rate of St_v with Ri becomes larger. The minimum $St_v \approx 0.065$ is obtained at $\phi = 0.0079$ and $Ri = 1$. The decreasing trend of St_v with either increasing Ri or decreasing ϕ can also be observed from the instantaneous temperature fields (figure 4).

Figure 14(b) shows that the St_v - Ri_{eff} curves of all cases are almost collapsed into the same curve when Ri is modified as the effective Richardson number (Ri_{eff}). For mixed convection around the solid cylinder, Ri accounts for the buoyancy force induced by heat transfer from the cylinder surface. However, for the cylinder array, the effective Ri should be considered due to the combined effects of the upward buoyancy-induced reverse flow within the array and the blockage effect of the array. Thus, the Ri_{eff} can be regarded as the multiplication of a shape factor r_s and Ri , with r_s closely related to the ϕ of the array. For compact arrays with a large ϕ , the combined effects are fairly small, i.e. $Ri_{eff} \approx Ri$. The permeability of the array increases as ϕ decreases. Thus, for the array with a relatively small ϕ or larger permeability, the upward buoyancy-induced reverse flow becomes stronger and the combined effects are much larger, i.e. $Ri_{eff} > Ri$. Here, the shape factor r_s is estimated somewhat empirically. For $\phi \approx 1$, $r_s \approx 1$. For smaller ϕ , $r_s > 1$. In the range of the investigated Ri and ϕ , the r_s is found to satisfy a linear relationship,

$$r_s = Ri_{eff}/Ri = -A_e\sqrt{\phi} + B_e \quad \text{for } \phi \leq 0.22, \quad (3.2)$$

with the coefficients of A_e and B_e being 3.69 and 3.02, respectively. The collapsed curve can be fitted into a polynomial relationship of $St_v = A_t Ri_{eff}^2 - B_t Ri_{eff} + C_t$, where the coefficients of A_t , B_t and C_t are 0.0077, 0.0498 and 0.143, respectively. Besides, the collapsed curves with respect to Ri_{eff} are only observed for St_v rather than $\overline{C_D}$ and $C_{L_{rms}}$. This is because St_v is mainly dependent on the geometry while other parameters are not only dependent on the geometry but also the recirculating wake.

The mean drag coefficients exerted on the array of cylinders also carry important information on flow through the array under the effects of opposing buoyancy. Locally, the integrated drag coefficient of an individual cylinder ($\overline{C_{dij}}$) can be calculated for each element. Since the variation of $\overline{C_{dij}}$ in the x direction is much larger than that in the y direction, $\overline{C_{dij}}$ of the cylinders in the fixed row ($j = 6$) are calculated and presented in figure 15. In general, the variation trends of $\overline{C_{dij}}$ with i are the same for different combinations of Ri and ϕ , i.e. $\overline{C_{dij}}$ decreases monotonically as the position of the cylinder approaches the rear of the array. This is due to the decreased velocity of the inertial flow as it penetrates deeper into the array and comes into the reverse buoyant flow. Also, for both

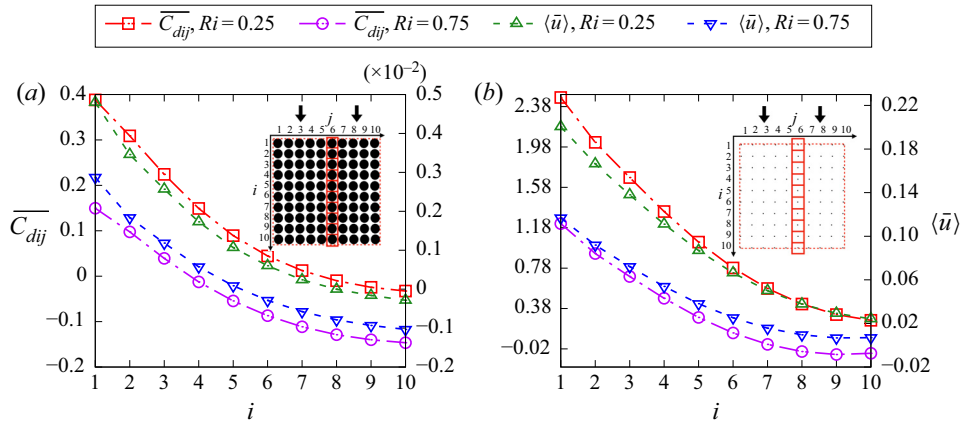


Figure 15. Variation of the drag coefficient of an individual cylinder (left y axis) and the Eulerian-averaged velocity (right y axis) with fixed $j = 6$ for (a) $\phi = 0.564$ and (b) $\phi = 0.00785$.

ϕ , \overline{C}_{dij} at a smaller Ri is larger than that at a larger Ri , demonstrating that the opposing buoyancy within the array weakens the drag of each cylinder. The \overline{C}_{dij} of cylinders close to the rear of the array can be negative since the buoyancy dominates over the inertial force. It is also seen that \overline{C}_{dij} at $\phi = 0.0079$ (figure 15b) is much larger than that at $\phi = 0.56$ (figure 15a) for fixed Ri . This seems contradictory to the observation that more fluid flows through the array for smaller ϕ . Nevertheless, it is reasonable because the viscous force exerted on an individual cylinder largely increases as its size decreases and the fluid is mainly convected through the array in an inertially dominated region outside of the viscous dominated region.

Besides, figure 15 also presents the Eulerian-averaged velocity ($\langle \bar{u} \rangle$) in a small square region defined by the centre of each cylinder and a side length of $d + s$. The small square region can be considered as a representative elementary volume (REV) from a macroscopic perspective of the porous body (the array). The variation trends of $\langle \bar{u} \rangle$ with increasing i are similar to those of \overline{C}_{dij} for different ϕ and Ri . For both ϕ , $\langle \bar{u} \rangle$ is smaller for larger Ri due to the reverse flow. For small ϕ , the velocity within the array is still small since fluid mainly flows around the array due to the non-trivial drag. It is also seen that the absolute value of $\langle \bar{u} \rangle$ at $\phi = 0.56$ is $\sim O(10^2)$ times smaller than that at $\phi = 0.0079$, while the absolute value of \overline{C}_{dij} at $\phi = 0.56$ is $\lesssim O(10)$ times smaller than that of $\phi = 0.0079$. This can be explained by the different permeabilities of the two arrays.

Considering the array of heated cylinders as a porous medium, the flow through the array in the x direction is described by the following equation based on Darcy's law:

$$u_f \phi_v = \frac{K}{\mu} \left[-\beta g (T_h - T_f) - \frac{\partial p_f}{\partial x} \right]. \quad (3.3)$$

Here the subscript f denotes the intrinsic quantity that is averaged over the fluid phase area of the porous medium in a REV based on the averaging volume theory (e.g. Whitaker 1967; Travkin & Catton 2001); ϕ_v is porosity that satisfies $\phi_v + \phi = 1$ and K is permeability. Since u_f is mainly affected by the drag force of the porous medium in the x direction, the variation of u_f in the y direction is much smaller than that in the x direction. It is noted that (3.3) is based on the averaged flow within the array, so the unsteady term is not included. The Darcy law is considered valid since the mean flow velocity within the array is quite small, resulting in a small pore Reynolds number (Re_p) no greater than ~ 2

for all the investigated cases (Nield & Bejan 2006). Consider $u_f = \langle \bar{u} \rangle$, K can be estimated for each REV. The estimated K does not vary much with x . Note that K can be both positive and negative due to the signs of the drag coefficient and the velocity. For $\phi = 0.56$, the averaged Darcy numbers ($\langle Da \rangle = \langle K \rangle / D^2$) are approximately 2.8×10^{-5} and 1.3×10^{-5} for $Ri = 0.25$ and $Ri = 0.75$, respectively; for $\phi = 0.0079$, the averaged $\langle Da \rangle$ are approximately 2.2×10^{-3} and 2.5×10^{-3} for $Ri = 0.25$ and $Ri = 0.75$, respectively. The same order of magnitude of the $\langle Da \rangle$ indicates that Ri does not have large effects on the overall permeability of the array.

This can also be demonstrated by using the semi-empirical formula (Tang *et al.* 2019) based on Darcy’s law for calculating the constant permeability of the array

$$K = \frac{D^2}{Nd\pi(k_0 - k_1\sqrt{R_d} + k_2R_d)}, \tag{3.4}$$

where N is the number of constituent elements; R_d is the Reynolds number of an individual cylinder calculated from $R_d = \langle \bar{U} \rangle d / \nu$ with $\langle \bar{U} \rangle$ being the Eulerian-averaged velocity (under forced convection) within the array. The geometry coefficients k_0, k_1, k_2 can be estimated from the $k_0-\phi, k_1-\phi, k_2-\phi$ relationships (Tang *et al.* 2019) via linear interpolation. The reasons for choosing this formula are that it was obtained from the drag force exerted on arrays of cylinders similar to the current geometry configuration and it was demonstrated to be more applicable to porous media with very small ϕ compared with the Carman–Kozeny equation. The estimated $Da = \langle Da \rangle$ ranges from 3.6×10^{-5} to 2.4×10^{-3} for ϕ decreasing from 0.56 to 0.0079, which is very similar to those obtained from averaging the local K .

We next investigate the integral parameters of force coefficients for the whole array. Figure 16(a) shows variations of $\overline{C_D}$ with Ri at representative fixed ϕ . For a solid square cylinder ($\phi = 1$), $\overline{C_D}$ initially decreases slightly and then increases with increasing Ri . This trend qualitatively matches that of flow around a solid circular or square cylinder under opposing buoyancy in the previous studies (Sharma & Eswaran 2004; Hu & Koochesfahani 2011), though different Re and Pr were considered. This trend mainly results from the combined effects of the viscous drag coefficient (C_{Dv}) and pressure drag coefficient (C_{Dp}). As shown in figure 17(a), C_{Dv} decreases with Ri due to the stronger reverse flow; while C_{Dp} increases with Ri since the flow separation occurs more upstream of the solid cylinder, forming a larger pair of vortexes. For flow around a solid bluff body at $Re = 100$, the total drag is mainly dominated by the pressure drag, therefore, the total drag tends to increase with Ri , except at very small Ri .

Contrastingly, for $\phi = 0.66$, $\overline{C_D}$ decreases quadratically with increasing Ri . This is because part of the pressure drag decreases with increasing Ri as the fluid flows through the array. For larger Ri , the flow separation occurs more upstream of the array so that part of the pressure drag still increases. The competence effects of the decreased and increased pressure drag give rise to the ultimate value. Also, the viscous drag for the compact array decreases more evidently than that of the solid square cylinder because of the larger surface area as well as the reverse flow within the array.

As ϕ further decreases, $\overline{C_D}$ decreases almost linearly with Ri . The fitting line with linear regression can be expressed as

$$\overline{C_D} = A_d Ri + B_d \quad \text{for } \phi \leq 0.22, \tag{3.5}$$

where the constant A_d decreases and B_d increases with decreasing ϕ . The constants A_d and B_d are approximately -1.5 and 1.8 , respectively, for $\phi \leq 0.026$. The quality of the linear regression fit is assessed by the coefficient of determination R^2 , which is no less than 0.99

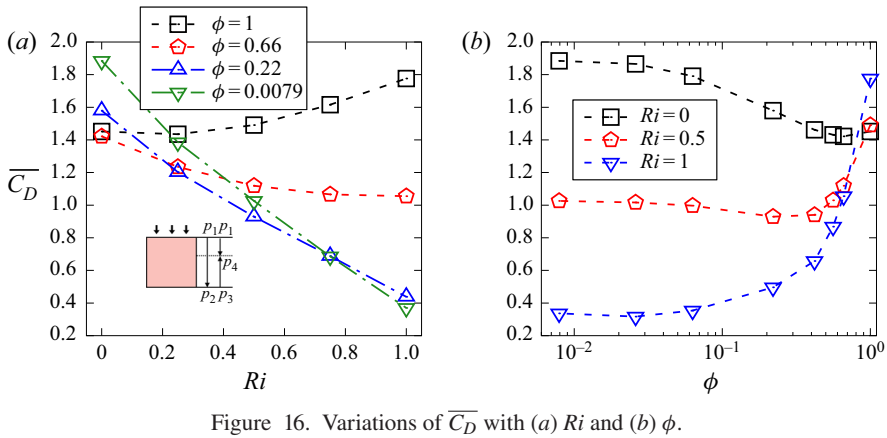


Figure 16. Variations of $\overline{C_D}$ with (a) Ri and (b) ϕ .

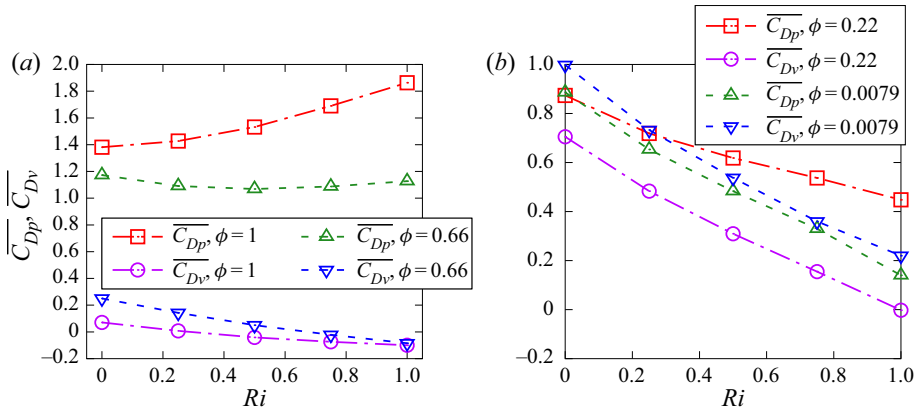


Figure 17. Pressure and viscous drag coefficients for (a) $\phi = 0.66, 1$ and (b) $\phi = 0.22, 0.00785$.

for the range of ϕ . Since C_{Dv} decreases almost linearly with Ri , the linear relationship of (3.5) indicates that the buoyancy within the array, rather than the vortex, has a major effect on C_{Dp} . The reason might be that the large recirculation can be detached from the array for $\phi \leq 0.22$. As the effect of the recirculating wake on the pressure drag is trivial, the pressure drag is mainly associated with the pressure difference between the front and rear surfaces of the array. An illustrative plot is also presented in figure 16(a), where the pressure difference without buoyancy force is $(p_1 - p_2)$ and with buoyancy force is $(p_1 - p_4)$. The magnitude of buoyancy ($|B|$) can be expressed as $|B| = p_3 - p_4$. Considering $p_2 = p_3$, we have $(p_1 - p_4) = (p_1 - p_2) - (p_4 - p_3) = (p_1 - p_2) - |B|$, which demonstrates that $(p_1 - p_4)$ is linear to $|B|$. As $|B|$ or Ri increases, $(p_1 - p_4)$ decreases, resulting in decreased pressure drag. Figure 17(b) also shows that C_{Dp} becomes comparable to C_{Dv} as ϕ decreases. Both C_{Dp} and C_{Dv} decrease linearly with Ri .

Figure 16(b) shows the variation of $\overline{C_D}$ with ϕ at fixed Ri . For all Ri , a decrease in $\overline{C_D}$ is observed as ϕ decreases from 1 to 0.66, which is mainly owing to the different peripheral shapes between a compact square array and a solid square cylinder (see figure 1b). For $Ri = 0$, $\overline{C_D}$ increases with decreasing ϕ when $\phi \leq 0.66$, which is due to the increasingly strong viscous force as the Reynolds number of an individual cylinder decreases. For ϕ smaller than a threshold value, the viscous drag can be dominant over the pressure drag,

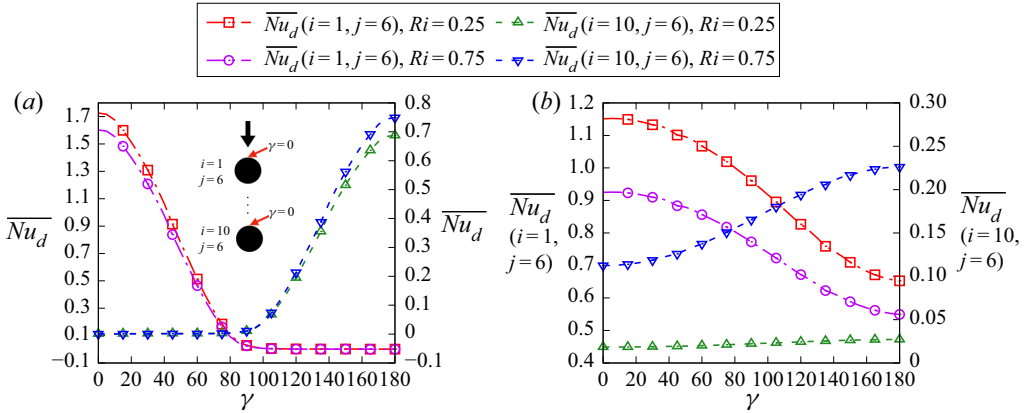


Figure 18. The variation of the local Nusselt number on the surface of an individual cylinder for (a) $\phi = 0.56$ and (b) $\phi = 0.00785$.

therefore, the total drag increases though the pressure drag still decreases with decreasing ϕ . Note that, for ϕ smaller than the low limit investigated here, \overline{C}_D is expected to decrease with decreasing ϕ since $\overline{C}_D \rightarrow 0$ as $\phi \rightarrow 0$. This would result in a peak \overline{C}_D in a wider range of ϕ , similar to those observed in the previous studies on flow through and around a permeable bluff body (Noymer, Glicksman & Devendran 1998; Tang *et al.* 2019).

For $Ri = 0.5$, \overline{C}_D first decreases and then slightly increases with decreasing ϕ . The firstly decreased drag is mainly due to the decreased pressure drag brought about by the opposing buoyancy. As ϕ further decreases, the viscous drag largely increases due to the reason stated above. The combined effects of the decreased pressure drag and the increased viscous drag give rise to the essentially unchanged \overline{C}_D at relatively small ϕ .

The trend of variation is more apparent for $Ri = 1$. It is observed that the valley \overline{C}_D occurs at a much smaller ϕ compared with the $Ri = 0.5$ case. The reason is that the pressure drag decreases to a greater extent as the buoyancy force gets stronger. Although the viscous drag increases with decreasing ϕ , its value largely decreases due to the stronger reverse flow in the array. Thus, the contribution from the viscous drag to the total drag is very small unless the pressure drag drops to a similar value, which usually occurs at very small ϕ while the upward buoyancy-induced reverse flow is stronger. Apart from this, the peak \overline{C}_D is also expected to be observed at a very small ϕ for the larger Ri cases.

3.3. The mean heat transfer coefficients

The mean heat transfer coefficients are also investigated. Figure 18 shows the variations of the local Nusselt number \overline{Nu}_d with angle γ (degree) on the rigid surfaces of two cylinders labelled as $(i, j) = (1, 6)$ and $(i, j) = (10, 6)$ for different ϕ and Ri (zero angle is on top of each cylinder). Only half of the \overline{Nu}_d distribution is shown since the flow around each cylinder in the column $j = 6$ is almost symmetric about the centreline of the array.

For relatively large ϕ (figure 18a), \overline{Nu}_d of the first cylinder ($i = 1$) decreases monotonically for $\gamma < 90$, and is approximately zero for $\gamma \geq 90$. On the contrary, \overline{Nu}_d of the tenth cylinder ($i = 10$) is around zero for $\gamma < 90$, and increases monotonically for $\gamma \geq 90$. This is because of the different directions of the incoming flow for the two cylinders. The fluid actually flows upward around the tenth cylinder due to buoyancy. Also, the flow velocity within the array is so small that convection hardly occurs. It is also

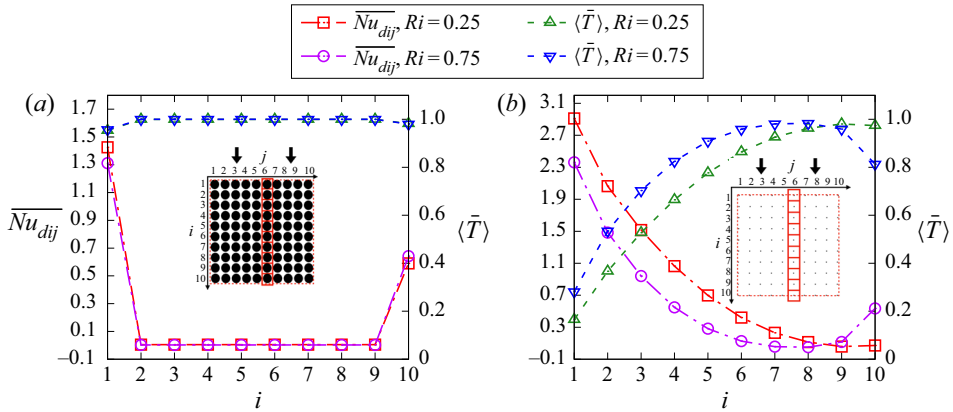


Figure 19. Variation of the Nusselt number of an individual cylinder (left y axis) and the Eulerian-averaged temperature (right y axis) with fixed $j = 6$ for (a) $\phi = 0.564$ and (b) $\phi = 0.00785$.

observed that \overline{Nu}_d of the first cylinder at $Ri = 0.25$ is slightly larger than that at $Ri = 0.75$, while the opposite trend is seen for the tenth cylinder. This demonstrates that the opposing buoyancy would decrease the heat transfer rate of the first cylinder and increase the heat transfer rate of the tenth cylinder. The \overline{Nu}_d of the first cylinder is twice larger than that of the tenth cylinder since the inertial flow is stronger than that of the buoyancy-induced reverse flow.

For small $\phi = 0.00785$ (figure 18b), the effects of buoyancy on the heat transfer rate are much larger. This is expected as discussed in § 3.1. At a smaller ϕ , the buoyancy-induced flow becomes stronger due to the lower blockage effect of the array, which thus has an enhanced effect on the heat transfer rate. For the first cylinder, \overline{Nu}_d decreases with γ . At $Ri = 0.25$, \overline{Nu}_d is noticeably larger than that at $Ri = 0.75$ for the whole range of γ . Compared with the compact array case, \overline{Nu}_d at $\gamma = 0$ is smaller, but \overline{Nu}_d at $\gamma \geq 90$ is much larger due to stronger convection. For the tenth cylinder, \overline{Nu}_d also shows the opposite variation trend with γ , i.e. \overline{Nu}_d increases with γ . At $Ri = 0.75$, \overline{Nu}_d is much higher than that at $Ri = 0.25$ because the buoyancy induced is stronger at the rear of the array for larger Ri . Overall, \overline{Nu}_d of the first cylinder is four times larger than that of the tenth cylinder due to the combined effects of the penetrating inertial flow and the buoyancy-induced reverse flow within the array.

The integrated Nusselt number over the surface of an individual cylinder can better reflect the overall trend of the heat transfer rate through the array. Figure 19(a) shows the variations of the Nusselt number for an individual cylinder \overline{Nu}_{dij} with i in the fixed column of $i = 6$. It is seen that \overline{Nu}_{dij} of the first and tenth cylinders are much larger than \overline{Nu}_{dij} of the other cylinders. The \overline{Nu}_{dij} of cylinders in the middle of the array are almost zero ($\sim 5.25 \times 10^{-3}$), which indicates that conduction is dominant over convection within the array. As also indicated in figure 18, \overline{Nu}_{dij} of the first cylinder is much larger than that of the tenth cylinder. The corresponding REV-averaged temperature $\langle \bar{T} \rangle$ first increases, then remains at high values for $2 \leq i \leq 9$, and finally slightly decreases due to the penetrating vortex at the rear of the array. Overall, both \overline{Nu}_{dij} and $\langle \bar{T} \rangle$ vary little among different Ri , implying that the heat is almost trapped within the compact array and is not affected by the buoyancy or the inertial forced flow.

Figure 19(b) shows $\overline{Nu_{dij}}$ at a very small ϕ . The effects of Ri on both $\overline{Nu_{dij}}$ and $\langle \bar{T} \rangle$ are much larger compared with the compact array case. For $Ri = 0.25$, $\overline{Nu_{dij}}$ continually decreases with i . Correspondingly, $\langle \bar{T} \rangle$ increases with i , implying that less heat is transferred from the cylinder to the fluid within the array. For $Ri = 0.75$, $\overline{Nu_{dij}}$ first decreases with i and then increases at the end of the array. Correspondingly, $\langle \bar{T} \rangle$ first increases with i and then decreases at the end of the array. The sudden increase in $\overline{Nu_{dij}}$ and decrease in $\langle \bar{T} \rangle$ is mainly owing to the entrainment of cold fluid at the rear surface of the array. In general, $\overline{Nu_{dij}}$ for the small ϕ case is larger than that for the compact array case. Also, it is observed that $\overline{Nu_{dij}}$ at $Ri = 0.25$ is larger than those at $Ri = 0.75$ for $i \leq 9$, while the opposite trend occurs for $i > 9$. This is because the inertial force is retarded as fluid flows through the array and the buoyancy is dominant over the inertial force for cylinders adjacent to the rear surface of the array.

Moreover, the corresponding variation trends between $\overline{Nu_{dij}}$ and $\langle \bar{T} \rangle$ indicate a theoretical relation between them. Considering the array of cylinders as a porous medium, the energy equation based on local thermal non-equilibrium can be expressed as (Nield & Bejan 2006)

$$\rho c \left(u_f \frac{\partial T_f}{\partial x} + v_f \frac{\partial T_f}{\partial y} \right) = k \left(\frac{\partial^2 T_f}{\partial x^2} + \frac{\partial^2 T_f}{\partial y^2} \right) + h_f(T_h - T_f), \quad (3.6)$$

where the subscript f is previously introduced in (3.3). The intrinsic-averaged temperature T_f in (3.6) is considered to be equal to the REV-averaged temperature $\langle \bar{T} \rangle$ from the direct numerical simulation. The local heat transfer coefficient h_f characterizes the heat transfer from the solid cylinders to the fluid phase in the porous medium. For the present flow configuration, T_f is largely influenced by advection related to u_f and the variation of T_f in the x direction is much larger than that in the y direction; thus, the energy equation can be simplified to

$$\rho c \left(u_f \frac{dT_f}{dx} \right) = k_f \frac{d^2 T_f}{dx^2} + h_f(T_h - T_f). \quad (3.7)$$

In order to simplify the analysis, u_f is assumed to be known and can be obtained from the direct numerical simulation. Thus, the general solution of (3.7) can be written as

$$T_f = c_1 e^{r_1 x} + c_2 e^{r_2 x} + c/b, \quad (3.8)$$

where $r_1 = 0.5(-a + \sqrt{a^2 - 4b})$, $r_2 = 0.5(-a - \sqrt{a^2 - 4b})$ with $a = -u_f \rho c_p/k$, $b = -h_f/k$ and $c = -h_f T_h/k$. The coefficients of c_1 and c_2 are obtained from the boundary conditions as

$$c_1 = T_i - T_h - c_2, \quad c_2 = \frac{T_o - T_h + T_h e^{r_1 D} - T_i e^{r_1 D}}{e^{r_2 D} - e^{r_1 D}}. \quad (3.9a,b)$$

Here, the temperature at the inlet boundary (T_i) and the outlet boundary (T_o) can also be obtained from the direct numerical simulation. It is seen that the relationship between h_f and T_f is very complicated with the effects of u_f .

We next investigate the mean Nusselt number (\overline{Nu}) of the whole array. From (2.8), we know that the Nusselt number definitions for the individual cylinder and the whole array are actually the integrals of the local Nusselt number over the individual cylinder surface and all the cylinder surfaces, respectively. For ease of comparison, the mean Nusselt number averaged over the enclosure surface area of an array or a solid square cylinder

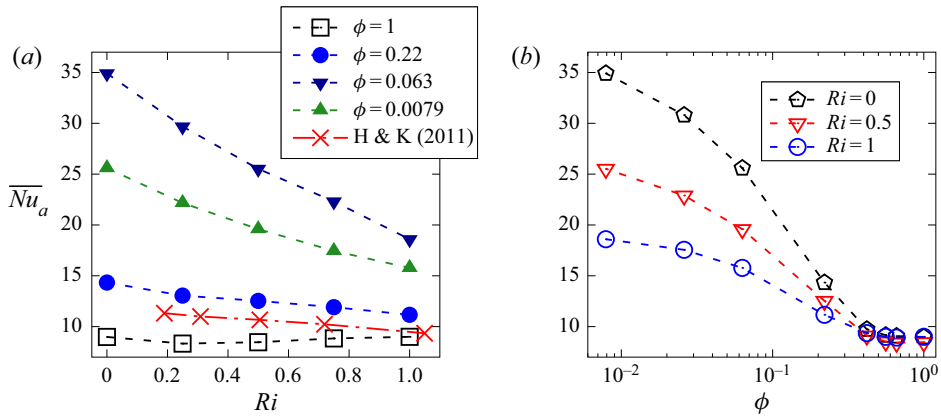


Figure 20. Variations of \overline{Nu}_a with (a) Ri and (b) ϕ . Here H & K (2011) is short for Hu & Koochesfahani (2011).

is calculated as $\overline{Nu}_a = \overline{Nu}/(4D)$ for all cases. Figure 20(a) shows the variation of \overline{Nu}_a with Ri at different ϕ . For $\phi = 1$, \overline{Nu}_a is approximately 10 for the range of Ri , which does not differ much from the experimental result for mixed convection around a solid circular cylinder (Hu & Koochesfahani 2011). For smaller $\phi \leq 0.22$, \overline{Nu}_a is noticeably larger for the investigated range of Ri . It is observed that \overline{Nu}_a decreases monotonically with increasing Ri . This seems contradictory to the expectation that more intense fluctuations at smaller ϕ would promote the overall heat transfer. However, the fluctuations mainly exist on the lateral sides and the wake region of the array instead of being around the individual cylinder surfaces in the array. The overall heat transfer rate is therefore significantly affected by the opposing buoyancy. Besides, larger opposing buoyancy also gives rise to a smaller frequency of the alternating flow behind the array, which takes less heat away from the array, as can be observed by comparing figure 4(b,e).

Also, it is found that \overline{Nu}_a decreases almost linearly with Ri for $\phi \leq 0.22$. The linear regression fit can be expressed as

$$\overline{Nu}_a = -A_n Ri + B_n \quad \text{for } \phi \leq 0.22. \quad (3.10)$$

The expression is similar to that of \overline{C}_D , except that the coefficients A_n and B_n here are largely dependent on ϕ . The corresponding coefficient of determinant R^2 is no less than 0.98 for $\phi \leq 0.22$, which increases with decreasing ϕ . The overall heat transfer of mixed convection can be decomposed of heat transfer from forced (positive effect) and buoyant convection (negative effect). As the buoyant convection increases, heat transfer of mixed convection decreases. Also, since the averaged temperature within the array increases, the heat transfer coefficient must decrease.

Figure 20(b) shows \overline{Nu}_a as a function of ϕ . For fixed Ri , \overline{Nu}_a is observed to increase with decreasing ϕ . The larger \overline{Nu}_a at smaller ϕ is mainly because of more fluid flowing through the array and convecting heat away from individual cylinders. Also, the interaction within the array is more intense, resulting in the transport of FHF further downstream. The increasing rate with decreasing ϕ however decreases at larger Ri since the opposing buoyancy has an opposite effect on heat transfer. It is also observed that, for larger ϕ , \overline{Nu}_a is almost the same for different Ri . This is because the heat exchange mainly occurs on the outer boundaries of the array and fluid hardly flows into the array. The inertial flow and opposing thermal buoyancy within the array do not have much influence on the heat

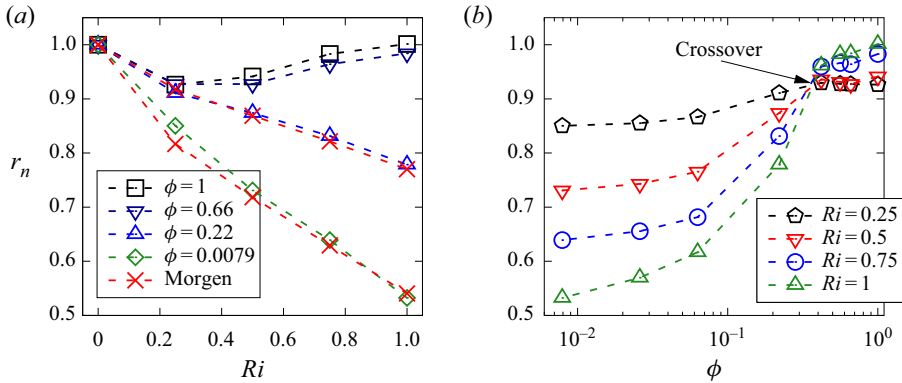


Figure 21. Variations of r_n with (a) Ri and (b) ϕ .

transfer rate. The averaged temperature also indicates that the heat transfer rate is much larger at small ϕ , but would decrease with increasing Ri .

Define the ratio $r_n = \overline{Nu}_a / \overline{Nu}_{af}$, with \overline{Nu}_{af} being the averaged mean Nusselt number for forced convection. Figure 21(a) presents variation of r_n with Ri . For $\phi = 1$, as Ri increases, r_n first decreases and then recovers at $Ri = 1$. Similar variation trends are also observed for relatively large $\phi \geq 0.42$, in which cases most of the fluid flows around the array. The decreased r_n is mainly owing to the decreased heat transfer rate on the lateral sides of the array. The increased r_n at relatively large Ri is mainly because of more ambient fluid being entrained into the wake region with an alternating separating and attaching flow, which promotes stronger heat exchange on the rear surface of the array. The increasing trend of \overline{Nu}_a with Ri can also be observed for flow over a triangular surface at large $Pr = 50$ (Chatterjee & Ray 2014) as well as for flow past two circular cylinders at a specific pitch-to-diameter (Salcedo *et al.* 2017). The monotonically decreasing trend of \overline{Nu}_a with Ri was also reported at larger $Re = 135$ (Hu & Koochesfahani 2011). It is noted that the decreasing trend easily exists for smaller Pr due to stronger heat conduction compared with heat convection, as demonstrated in the previous studies (e.g. Morgan 1975; Chang & Sa 1990; Sharma & Eswaran 2004) on flow around a heated solid square cylinder. However, one can also find the exception of Fornarelli *et al.* (2017) that the global Nusselt number increases with Ri at $Pr = 0.7$ for flow past an array of in-line cylinders, which is on account of the increased fluctuating intensity.

For $\phi \leq 0.22$, r_n decreases almost linearly with increasing Ri and is smaller than those of compact arrays or the solid square cylinder. The linear fitting can be obtained as

$$\overline{Nu}_a / \overline{Nu}_{af} = 1 - (A_r \phi + B_r) Ri \quad \text{for } \phi \leq 0.22, \quad (3.11)$$

with R^2 no less than 0.98. The constant coefficients A_r and B_r are -1.175 and 0.4694 , respectively. Considering that $Ri = Gr/Re^2$, (3.11) is similar to the Morgen model expressed as $r_n = (1 - AGr^{m/n} / Re)^n$. The constants A , m/n and n were set as 0.548 , 0.531 and 0.471 , respectively, as suggested by Morgan (1975). The results from the Morgen model are different from those of Chang & Sa (1990) and the present result. The limitation of the Morgen model for contra flows comes from the complex secondary flows, which significantly affects the predicted results. However, the Morgen model seems to well predict r_n for $\phi \leq 0.22$ with the same A and m/n but adjusted values of n , as presented in figure 21(a). The percent error is no greater than 5% by using the least

square fitting. A linear relationship is also found for the coefficient n in the Morgen model as $n = -0.722\sqrt{\phi} + 0.543$ for $\phi \leq 0.22$.

Figure 21(b) presents variation of r_n with ϕ at four fixed Ri . Contrary to the variation trend of \overline{Nu}_a (figure 20b), r_n decreases with decreasing ϕ for each Ri . This is because the increasing \overline{Nu}_a is largely dependent on the increasing \overline{Nu}_{af} with decreasing ϕ . As the effects of \overline{Nu}_{af} are removed, the decreasing ϕ promotes to larger opposing buoyancy although Ri is fixed. The four lines in figure 21(b) also reveal a crossover point ($\phi_c = 0.38$, $r_{nc} = 0.92$) that when $\phi \leq \phi_c$, r_n increases with Ri and the difference among the presented Ri is evidently large; for $\phi > \phi_c$, r_n decreases with Ri and the difference among various Ri is much smaller. This also applies to \overline{Nu}_a presented in figure 20(b). Also, the crossover point clarifies the observations in figure 21(a). When $\phi \leq \phi_c$, the linear relationship between r_n and Ri approximately applies, and r_n can be roughly estimated by (3.11). For $\phi > \phi_c$, the trend is nonlinear. The critical ϕ_c also somewhat corresponds to the change point of the variation trends for \overline{C}_D (figure 16).

4. Summary and conclusions

A series of numerical simulations are performed for unsteady mixed convection through and around arrays of 10×10 heated circular cylinders. The instantaneous flow and heat transfer characteristics are found to be significantly modified by ϕ and Ri . In the investigated ranges of ϕ and Ri , six flow patterns are identified based on the mean recirculation regions, i.e. P-1: symmetric flow with near-wake vortexes; P-2: unsymmetric flow with near-wake vortexes; P-3: unsymmetric flow with near-wake vortexes and lateral vortexes; P-4: unsymmetric flow with near-wake vortexes, lateral vortexes and detached far-wake vortexes; P-5: unsymmetric flow with near-wake vortexes, lateral vortexes and connected far-wake vortexes (with near-wake vortexes); P-6: unsymmetric flow with near-wake vortexes, lateral vortexes, connected far-wake vortexes and a small vortex pair between lateral vortexes and near-wake vortexes. The first three patterns mainly appear at relatively small Ri and/or large ϕ , which were also observed in the previous studies (see § 1) for flow around a solid cylinder. The last three patterns mainly exist at relatively large Ri and/or small ϕ . Although previous experiments (Hu & Koochesfahani 2011; Guillén *et al.* 2014) showed the appearance of large recirculation behind a solid cylinder at large Ri , patterns P-4 to P-6 were not previously reported.

The formation of the large recirculation in patterns P-4 to P-6 is found to be correlated with the instability of the fluctuating flow, which is largely affected by the FHF on the lateral sides of the array. This is different from the near-wake vortex pair, which is mainly formed by the flow separation from the rigid surface of the solid square cylinder or the extended shear layer behind the array. For relatively small ϕ , the instability develops from the lateral sides of the array, which is accumulated and transported to the far wake to form a large recirculation that is detached from the near-wake vortexes. As ϕ further decreases, the large recirculation is connected with the near-wake vortexes due to larger flow instability.

Behaviours of the fluctuating force coefficients of the whole array are also found to be closely related to the mean recirculation. The phase portrait of C_D and C_L shows that the flow becomes more noisy as Ri increases as well as ϕ decreases. The PSD shows the flow transition from periodic to quasi-periodic or noisy subharmonic as Ri increases (ϕ decreases) for fixed ϕ (Ri). The amplitude of C_L increases monotonically with Ri for fixed ϕ and varies non-monotonically with ϕ for fixed Ri . It is found that St_v decreases with

increasing Ri . Considering the effective Richardson number (Ri_{eff}) based on the geometry of the array, the St_v-Ri_{eff} curves of all cases are almost collapsed into the same curve.

The mean drag and mean heat transfer coefficients are also analysed. Both the local drag coefficient and the REV-averaged velocity are found to decrease monotonically with the streamwise distance. The permeability is estimated from the local drag and averaged velocity, which does not vary much for fixed ϕ . The corresponding relation between the local Nusselt number and the REV-averaged temperature is also revealed. Over the investigated ranges of Ri and ϕ , the global $\overline{C_D}$ is found to decrease greatly with increasing Ri , the decreasing rate of which increases as ϕ becomes smaller. Also, the global $\overline{Nu_a}$, at large ϕ , initially decreases and then increases with Ri , while at small $\phi \leq 0.22$, $\overline{Nu_a}$ decreases almost linearly with Ri , similar to $\overline{C_D}$.

Finally, it is noted that the geometry configuration in the current study is somewhat specific due to the in-line arrangement as well as the circular shape of the constituent elements. A preliminary study on the effects of different arrangements is also conducted. It is found that, for relatively large ϕ , the characteristics of flow and heat transfer through and around a staggered array of cylinders are similar to those of flow past an in-line array of cylinders, as expected since the fluid mainly flows around the array. For smaller ϕ , the effect of staggered arrangements on the flow becomes more prominent since it alters the path as well as the permeability of the flow through the array. Besides, the flow is expected to present three-dimensional behaviours at relatively small ϕ as well as relatively large Ri due to the fluctuations with different amplitudes. Therefore, the transition behaviour of three-dimensional flow with respect to Ri for more complicated arrangements of cylinder arrays (e.g. staggered and random) as well as other shapes of constituent elements will be considered in the future.

Funding. The authors would like to thank financial support from NSFC (Grant Nos. 12172163, 12002148 and 11672124), the Shenzhen Peacock Plan (KQTD2016022620054656) and Guangdong Provincial Key Laboratory of Turbulence Research and Applications (Grant No. 2019B21203001). This work is supported by the Center for Computational Science and Engineering of Southern University of Science and Technology.

Declaration of interests. The authors report no conflict of interest.

Author ORCIDs.

 Jianhui Li <https://orcid.org/0000-0002-2492-2646>;

 Peng Yu <https://orcid.org/0000-0003-2073-7512>.

Author contributions. T.T. and Z.L. contributed equally to this work.

Appendix A

A.1. Mesh, time step and domain independence tests

Figure 22 shows a typical mesh for the present calculations. Region I represents the area of the array with 10×10 circular cylinders, as shown by the zoom-in plot. Each circular cylinder resides at the centre of a small square patch where O-type mesh is used. The mesh size stretches from the cylinder surface to the small patch boundary. Region II is the area outside of the array with the vertical distance $41D$ from the inlet to the downstream side. The mesh size stretches from the array enclosure surface to the computational boundaries. Region III is the area in the far wake with a vertical length of $40D$ from the right boundary of region II to the outlet boundary. The hyperbolic tangent function is used for stretching cell sizes between limits.

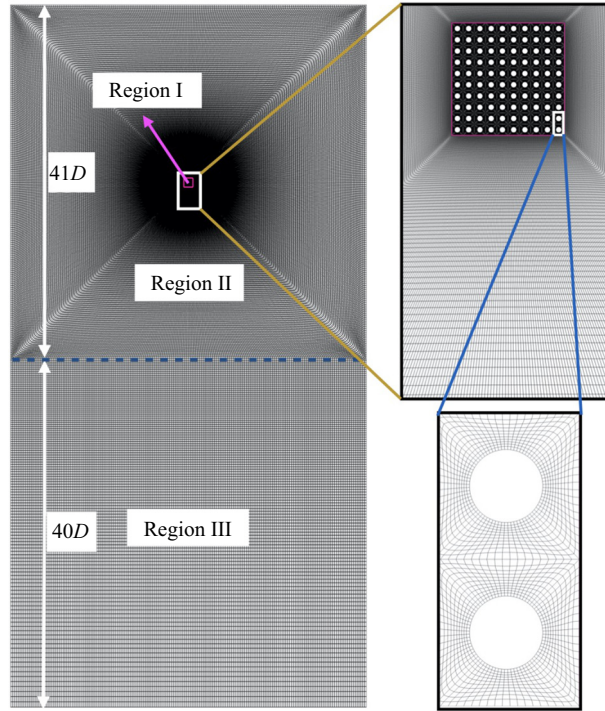


Figure 22. Illustration of the computational grid for $\phi = 0.22$.

Case	Grids (I)	Grids (II)	Grids (III)	$\overline{C_D}$	$C_{L'rms}$	St	\overline{Nu}
1	80 × 560	134 × 560	89 × 140	1.196	0.2718	0.1345	8.506
2*	80 × 760	179 × 760	119 × 190	1.195	0.2715	0.1345	8.500
3	80 × 960	224 × 960	149 × 240	1.194	0.2712	0.1344	8.499

Table 1. Comparisons of the variables for different grid sizes. Grids (I), grids (II) and grids (III) denote the number of grids in regions I, II and III shown in figure 22.

The mesh, time step and domain independence tests are performed under a typical unsteady mixed convection condition of $Re = 100$, $Pr = 7$, $s/d = 0.2$, $Ri = 0.25$. The independence tests for other Pr , s/d and Ri show similar results. Table 1 shows the grid independence study for a fixed time step of 0.0005 and a fixed domain with $N_L = N_R = N_T = 20D$ and $N_B = 60D$. Different sets of grids are used in each region as indicated. The percent differences between the first and second and between the second and third sets of grids are no greater than 0.11 % for all variables, which demonstrates that all meshes are sufficiently fine for the current problem. The overall difference for all variables between second and third meshes is slightly smaller, thus, the mesh in case 2* is adopted.

The independence test for the time step is shown in table 2. Three dimensionless time steps which successively decrease by half are used. The differences between cases 1 and 2* and between cases 2* and 3 are no greater than 0.2 % and 0.1 %, respectively. The results show that the time discretization step of case 2* is sufficiently small for accuracy as well as saving computational resources.

Case	δt^*	$\overline{C_D}$	$C_{L'rms}$	St	\overline{Nu}
1	0.001	1.195	0.2719	0.1348	8.501
2*	0.0005	1.195	0.2715	0.1345	8.500
3	0.00025	1.195	0.2712	0.1342	8.498

Table 2. Comparisons of the variables for different time-step sizes.

Case	N_L	N_B	$\overline{C_D}$	$C_{L'rms}$	St	\overline{Nu}
1	10D	60D	1.230	0.2759	0.1373	8.560
2*	20D	60D	1.195	0.2715	0.1345	8.500
3	30D	60D	1.195	0.2737	0.1341	8.495
4	20D	50D	1.195	0.2735	0.1347	8.495
5	20D	70D	1.195	0.2714	0.1344	8.497

Table 3. Comparisons of the variables for different domain sizes.

For the domain independence test, calculations are performed with five sets of domains, as indicated in table 3. From cases 1 to 3, the lateral length (N_L) increases from 10D to 30D while the downstream length (N_B) is fixed at 60D. All variables decrease with N_L with a larger successive discrepancy between cases 1 and 2*. The percent difference between cases 2* and 3 is no greater than 0.8 % for all variables, demonstrating that $N_L = 20D$ is sufficiently large. For fixed N_L , cases 4, 2*, 5 show N_B increasing from 50D to 70D. The differences between cases 2* and 4 are no greater than 0.8 % and the differences between 2* and 5 are no greater than 0.1 %. Therefore, the domain of case 2* can be used for the present study.

A.2. Validation

The validation is firstly performed for the steady flow around a circular cylinder under forced convection. The steady regime is chosen here because the Reynolds number of an individual cylinder ($Re_d = U_\infty d/\nu$) within the array ranges from 1 to 9.2 corresponding to fixed $Re = 100$ and varying ϕ . The Re_d is even smaller if the averaged velocity within the array is used as the reference velocity scale. Table 4 shows the C_D and Nu_a at various Re for the present study as well as several previous studies. For the C_D , the percent errors estimated from the literature results (Tritton 1959; Takami & Keller 1969; Dennis & Chang 1970) range from 0 to 3.1 %, 1 % to 4.2 %, 1.1 % to 2.2 % and 0.6 % to 5 % for $Re = 10, 20, 30$ and 40, respectively. For the Nu_a , the percent errors computed from the previous results (Dennis, Hudson & Smith 1968; Jafroudi & Yang 1986; Bharti, Chhabra & Eswaran 2007; Biswas & Sarkar 2009) differ from 1 % to 3.1 %, 0.4 % to 4.6 %, 0 to 1.4 % and 0 to 6.6 % for $Re = 10, 20, 30$ and 40, respectively. Therefore, the current numerical scheme is considered valid and the grid resolution around each circular cylinder is sufficiently fine for the rest of the computations.

The local Nu is then calculated for steady flow around a solid circular cylinder considering both forced convection and mixed convection with aiding buoyancy. Figure 23(a) shows that the present results agree well with the previous studies (Dennis *et al.* 1968; Biswas & Sarkar 2009) for $Re = 10$. At $Re = 20$, the present local Nu compares well with that of Biswas & Sarkar (2009) for the whole range of angle (γ) but is slightly

	$Re = 10$	$Re = 20$	$Re = 30$	$Re = 40$
<i>Drag coefficient (C_D)</i>				
Present	2.78	2.02	1.70	1.51
Takami & Keller (1969)	2.78	2.00	1.72	1.52
Dennis & Chang (1970)	2.87	2.05	—	1.54
Tritton (1959)	2.79	2.11	1.74	1.59
<i>Average Nusselt number (Nu_a)</i>				
Present	1.84	2.44	2.89	3.25
Biswas & Sarkar (2009)	1.86	2.45	2.89	3.25
Jafroudi & Yang (1986)	1.82	2.43	2.85	3.20
Dennis <i>et al.</i> (1968)	1.90	2.56	—	3.48
Bharti <i>et al.</i> (2007)	1.86	2.47	—	3.28

Table 4. Validation of steady flow around a circular cylinder with forced convection ($Ri = 0$) by comparing results with those in the literature at $Pr = 0.7$.

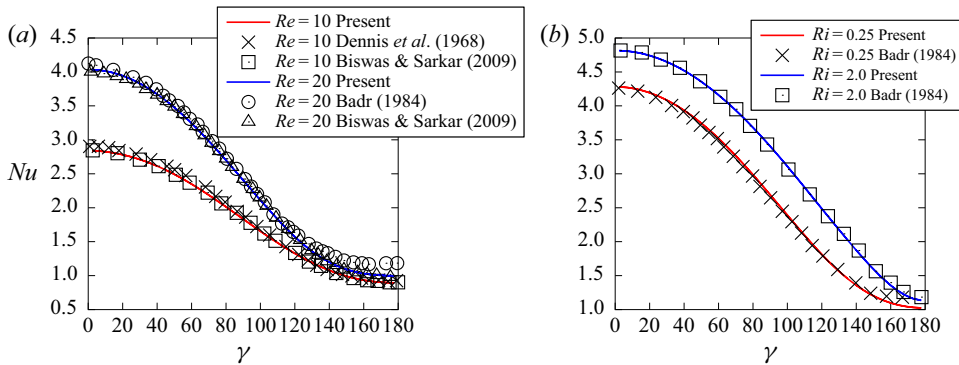


Figure 23. Validation of local Nu on the cylinder surface at $Pr = 0.7$ for (a) forced convection ($Ri = 0$) and (b) parallel flow with aiding buoyancy at $Re = 20$.

smaller than that of Badr (1984) at angles from 140 to 180°. Figure 23(b) presents that the current results overall match well with those from Badr (1984) for different Ri at fixed $Re = 20$. The present Nu for $Ri = 0.25$ is slightly smaller than the literature result (Badr 1984) for $160 \leq \gamma \leq 180$ (degrees).

It is also necessary to validate the numerical method for the unsteady flow around a solid square cylinder with side length D to capture accurately the array-scale vortex shedding. Table 5 shows the comparisons of the present results with those from the literature for forced convection at $Pr = 0.7$ and $Re = 100$. The $\overline{C_D}$ of the present study agrees well with the previous two-dimensional numerical results provided by Sohankar *et al.* (1997) and Sen *et al.* (2011) as well as the three-dimensional results from Saha *et al.* (2003) and Mahir & Altaç (2019) with the percent errors ranging from 1.2 % to 5.2 %. The comparison with three-dimensional results is considered meaningful since the three-dimensional effects are fairly small at $Re = 100$. The present $C_{L'rms}$ compares well with the previous results (Sharma & Eswaran 2004; Sen *et al.* 2011; Mahir & Altaç 2019), the percent errors of which are from 3.4 % to 5.2 %. The $C_{L'rms}$ of Sohankar *et al.* (1997) however is much smaller than the others. The St also shows a good agreement between the current and literature results (Okajima 1982; Sharma & Eswaran 2004; Sen *et al.* 2011) with the percent errors varying from 1.4 % to 5.2 %. The \overline{Nu} shows the best consistency with the

<i>Mean drag coefficient ($\overline{C_D}$)</i>		<i>The r.m.s. lift coefficient ($C_{L,rms}$)</i>	
Present	1.450	Present	0.182
Sohankar, Norberg & Davidson (1997)	1.478	Sharma & Eswaran (2004)	0.192
Sen <i>et al.</i> (2011)	1.529	Sohankar <i>et al.</i> (1997)	0.153
Saha, Biswas & Muralidhar (2003) (3D)	1.496	Sen <i>et al.</i> (2011)	0.191
Mahir & Altaç (2019) (3D)	1.433	Mahir & Altaç (2019) (3D)	0.176
<i>Strouhal number (St)</i>		<i>Mean Nusselt number (\overline{Nu})</i>	
Present	0.144	Present	4.000
Okajima (1982)	0.142	Sharma & Eswaran (2004)	4.010
Sen <i>et al.</i> (2011)	0.149	Mahir & Altaç (2019)	4.020
Sharma & Eswaran (2004)	0.152	Mahir & Altaç (2019) (3D)	4.032

Table 5. Validation of unsteady flow around a square cylinder with forced convection ($Ri = 0$) by comparing results with those in the literature at $Pr = 0.7$ and $Re = 100$. Here 3D is short for three dimensional.

previous results (Sharma & Eswaran 2004; Mahir & Altaç 2019) among the calculated variables, with the percent errors between 0.25 % and 0.8 %.

REFERENCES

- ANIRUDH, K. & DHINAKARAN, S. 2018 On the onset of vortex shedding past a two-dimensional porous square cylinder. *J. Wind Engng Ind. Aerodyn.* **179**, 200–214.
- BADR, H.M. 1984 Laminar combined convection from a horizontal cylinder—parallel and contra flow regimes. *Intl J. Heat Mass Transfer* **27** (1), 15–27.
- BHARTI, R.P., CHHABRA, R.P. & ESWARAN, V. 2007 A numerical study of the steady forced convection heat transfer from an unconfined circular cylinder. *Heat Mass Transfer* **43** (7), 639–648.
- BISWAS, G. & SARKAR, S. 2009 Effect of thermal buoyancy on vortex shedding past a circular cylinder in cross-flow at low Reynolds numbers. *Intl J. Heat Mass Transfer* **52** (7–8), 1897–1912.
- CHAKKINGAL, M., DE GEUS, J., KENJEREŠ, S., ATAIEI-DADAVI, I., TUMMERS, M.J. & KLEIJN, C.R. 2020 Assisting and opposing mixed convection with conjugate heat transfer in a differentially heated cavity filled with coarse-grained porous media. *Intl Commun. Heat Mass Transfer* **111**, 104457.
- CHANG, K.-S. & SA, J.-Y. 1990 The effect of buoyancy on vortex shedding in the near wake of a circular cylinder. *J. Fluid Mech.* **220**, 253–266.
- CHATTERJEE, D. & MONDAL, B. 2011 Effect of thermal buoyancy on vortex shedding behind a square cylinder in cross flow at low Reynolds numbers. *Intl J. Heat Mass Transfer* **54** (25–26), 5262–5274.
- CHATTERJEE, D. & RAY, S. 2014 Influence of thermal buoyancy on boundary layer separation over a triangular surface. *Intl J. Heat Mass Transfer* **79**, 769–782.
- DENNIS, S.C.R. & CHANG, G.-Z. 1970 Numerical solutions for steady flow past a circular cylinder at Reynolds numbers up to 100. *J. Fluid Mech.* **42** (3), 471–489.
- DENNIS, S.C.R., HUDSON, J.D. & SMITH, N. 1968 Steady laminar forced convection from a circular cylinder at low Reynolds numbers. *Phys. Fluids* **11** (5), 933–940.
- FORNARELLI, F., LIPPOLIS, A. & ORESTA, P. 2017 Buoyancy effect on the flow pattern and the thermal performance of an array of circular cylinders. *Trans. ASME J. Heat Transfer* **139** (2), 022501.
- FRISCH, U. & KOLMOGOROV, A.N. 1995 *Turbulence: the Legacy of AN Kolmogorov*. Cambridge University Press.
- GANDIKOTA, G., AMIROUDINE, S., CHATTERJEE, D. & BISWAS, G. 2010 The effect of aiding/opposing buoyancy on two-dimensional laminar flow across a circular cylinder. *Numer. Heat Transfer* **58** (5), 385–402.
- GOLDMAN, D. & JALURIA, Y. 1986 Effect of opposing buoyancy on the flow in free and wall jets. *J. Fluid Mech.* **166**, 41–56.
- GUILLÉN, I., TREVIÑO, C. & MARTÍNEZ-SUÁSTEGUI, L. 2014 Unsteady laminar mixed convection heat transfer from a horizontal isothermal cylinder in contra-flow: buoyancy and wall proximity effects on the flow response and wake structure. *Exp. Therm. Fluid Sci.* **52**, 30–46.

- HU, H. & KOOCHESEFAHANI, M.M. 2011 Thermal effects on the wake of a heated circular cylinder operating in mixed convection regime. *J. Fluid Mech.* **685**, 235–270.
- ISSA, R.I. 1986 Solution of the implicitly discretised fluid flow equations by operator-splitting. *J. Comput. Phys.* **62** (1), 40–65.
- JAFROUDI, H. & YANG, H.T. 1986 Steady laminar forced convection from a circular cylinder. *J. Comput. Phys.* **65** (1), 46–56.
- LEDDA, P.G., SICONOLFI, L., VIOLA, F., CAMARRI, S. & GALLAIRE, F. 2019 Flow dynamics of a dandelion pappus: a linear stability approach. *Phys. Rev. Fluids* **4** (7), 071901.
- LIU, S., JIANG, L., CHONG, K.L., ZHU, X., WAN, Z.-H., VERZICCO, R., STEVENS, R.J.A.M., LOHSE, D. & SUN, C. 2020 From Rayleigh–Bénard convection to porous-media convection: how porosity affects heat transfer and flow structure. *J. Fluid Mech.* **895**, A18.
- MAHIR, N. & ALTAÇ, Z. 2019 Numerical investigation of flow and combined natural-forced convection from an isothermal square cylinder in cross flow. *Intl J. Heat Fluid Flow* **75**, 103–121.
- MAKINDE, O.D. & OLANREWAJU, P.O. 2010 Buoyancy effects on thermal boundary layer over a vertical plate with a convective surface boundary condition. *Trans. ASME J. Fluids Engng* **132** (4), 044502.
- MORGAN, V.T. 1975 The overall convective heat transfer from smooth circular cylinders. In *Advances in Heat Transfer* (ed. T.F. Irvine & J.P. Hartnett.), vol. 11, pp. 199–264. Elsevier.
- NICOLLE, A. & EAMES, I. 2011 Numerical study of flow through and around a circular array of cylinders. *J. Fluid Mech.* **679**, 1–31.
- NIELD, D.A. & BEJAN, A. 2006 *Convection in Porous Media*, vol. 3. Springer.
- NOYMER, P.D., GLICKSMAN, L.R. & DEVENDRAN, A. 1998 Drag on a permeable cylinder in steady flow at moderate Reynolds numbers. *Chem. Engng Sci.* **53** (16), 2859–2869.
- OKAJIMA, A. 1982 Strouhal numbers of rectangular cylinders. *J. Fluid Mech.* **123**, 379–398.
- PATNAIK, B.S.V., NARAYANA, P.A.A. & SEETHARAMU, K.N. 1999 Numerical simulation of vortex shedding past a circular cylinder under the influence of buoyancy. *Intl J. Heat Mass Transfer* **42** (18), 3495–3507.
- SAHA, A.K., BISWAS, G. & MURALIDHAR, K. 2003 Three-dimensional study of flow past a square cylinder at low Reynolds numbers. *Intl J. Heat Fluid Flow* **24** (1), 54–66.
- SALCEDO, E., CAJAS, J.C., TREVIÑO, C. & MARTÍNEZ-SUÁSTEGUI, L. 2017 Numerical investigation of mixed convection heat transfer from two isothermal circular cylinders in tandem arrangement: buoyancy, spacing ratio, and confinement effects. *Theor. Comput. Fluid Dyn.* **31** (2), 159–187.
- SALIMPOUR, E. 2019 A numerical study on the fluid flow and heat transfer from a horizontal circular cylinder under mixed convection. *Intl J. Heat Mass Transfer* **131**, 365–374.
- SARKAR, S., GANGULY, S. & DALAL, A. 2013 Buoyancy driven flow and heat transfer of nanofluids past a square cylinder in vertically upward flow. *Intl J. Heat Mass Transfer* **59**, 433–450.
- SEN, S., MITTAL, S. & BISWAS, G. 2011 Flow past a square cylinder at low Reynolds numbers. *Intl J. Numer. Meth. Fluids* **67** (9), 1160–1174.
- SHARMA, A. & ESWARAN, V. 2004 Effect of aiding and opposing buoyancy on the heat and fluid flow across a square cylinder at $Re = 100$. *Numer. Heat Transfer* **45** (6), 601–624.
- SHARMA, A. & ESWARAN, V. 2005 Effect of channel-confinement and aiding/opposing buoyancy on the two-dimensional laminar flow and heat transfer across a square cylinder. *Intl J. Heat Mass Transfer* **48** (25–26), 5310–5322.
- SOHANKAR, A., NORBERG, C. & DAVIDSON, L. 1997 Numerical simulation of unsteady low-Reynolds number flow around rectangular cylinders at incidence. *J. Wind Engng Ind. Aerodyn.* **69**, 189–201.
- TADDEI, S., MANES, C. & GANAPATHISUBRAMANI, B. 2016 Characterisation of drag and wake properties of canopy patches immersed in turbulent boundary layers. *J. Fluid Mech.* **798**, 27–49.
- TAKAMI, H. & KELLER, H.B. 1969 Steady two-dimensional viscous flow of an incompressible fluid past a circular cylinder. *Phys. Fluids* **12** (12), II–51.
- TANG, T., YU, P., SHAN, X., CHEN, H. & SU, J. 2019 Investigation of drag properties for flow through and around square arrays of cylinders at low Reynolds numbers. *Chem. Engng Sci.* **199**, 285–301.
- TANG, T., YU, P., SHAN, X., LI, J. & YU, S. 2020 On the transition behavior of laminar flow through and around a multi-cylinder array. *Phys. Fluids* **32** (1), 013601.
- TRAVKIN, V.S. & CATTON, I. 2001 Transport phenomena in heterogeneous media based on volume averaging theory. In *Advances in Heat Transfer* (ed. H.G. Garg & C.A. Hales), vol. 34, pp. 1–144. Elsevier.
- TRITTON, D.J. 1959 Experiments on the flow past a circular cylinder at low Reynolds numbers. *J. Fluid Mech.* **6** (4), 547–567.
- VIJAYBABU, T.R., ANIRUDH, K. & DHINAKARAN, S. 2017 Mixed convective heat transfer from a permeable square cylinder: a lattice Boltzmann analysis. *Intl J. Heat Mass Transfer* **115**, 854–870.

Opposing-buoyancy mixed convection through cylinder arrays

- VIJAYBABU, T.R., ANIRUDH, K. & DHINAKARAN, S. 2018 Lattice Boltzmann simulations of flow and heat transfer from a permeable triangular cylinder under the influence of aiding buoyancy. *Intl J. Heat Mass Transfer* **117**, 799–817.
- WHITAKER, S. 1967 Diffusion and dispersion in porous media. *AIChE J.* **13** (3), 420–427.
- YU, S., YU, P. & TANG, T. 2018 Effect of thermal buoyancy on flow and heat transfer around a permeable circular cylinder with internal heat generation. *Intl J. Heat Mass Transfer* **126**, 1143–1163.
- ZARGARTALEBI, M. & AZAIEZ, J. 2019 Flow dynamics and heat transfer in partially porous microchannel heat sinks. *J. Fluid Mech.* **875**, 1035–1057.
- ZDRAVKOVICH, M.M. 1997 *Flow Around Circular Cylinders. Fundamentals*, vol. 1. Oxford University Press.
- ZONG, L. & NEPF, H. 2012 Vortex development behind a finite porous obstruction in a channel. *J. Fluid Mech.* **691**, 368–391.